UNC
N.C. CANCER HOSPITAL
LINEBERGER COMPREHENSIVE CANCER CENTER

March 21, 2013

Antonietta J. Reyes
U.S. Department of Energy
Closeout-Contract 202-5865372
antonietta.reyes@hq.doe.gov

RE: DE-FG02-ER64723 – Phase III – Research Final Report

Dear Ms. Reyes:

Attached is the final report for Dr. Lin's project entitled "Collaborative Initiative in Biomedical Imaging to Study Complex Diseases" with agency no. DE-FG02-ER64723. We have also included the quarterly progress report for the period of 01/01/2012 - 03/31/2012 for the above mentioned grant.

If you have any questions or need additional information, please contact Mark Kramer at 919-966-2629, or by email at mark_kramer@med.unc.edu.

Sincerely,

Mark Kramer
Assistant Director of Research Administration
Lineberger Comprehensive Cancer Center
Center for Translational Research
Institute for Nanomedicine
Center for AIDS Research
Biomedical Research Imaging Center
University of North Carolina at Chapel Hill
450 West Drive, CB#7295
Chapel Hill, NC 27599-7295
Phone 919-966-2629

# Cost Table

Grant No. DE-FG02-ER64723
Date Prepared: 03/31/2012

For Quarter Ending: 03/31/2012

| Quarter= | GFY11Q2 | GFY11Q3 | GFY11Q4 | GFY12Q1 | GFY12Q2 | GFY12Q3 | | | Comments |
|---|---|---|---|---|---|---|---|---|---|
| Ending= | 12/31/2010 | 3/31/2011 | 6/30/2011 | 9/30/2011 | 12/31/2011 | 3/31/2012 | | | References |
| Funds/Costs, $k | $122,888 | $111,013 | $111,014 | $111,014 | $0 | $0 | | | |
| | | | | | | | | | |
| Cum. Obligated by DOE, | $122,888 | $111,013 | $111,014 | $111,014 | $0 | $0 | | | |
| | | | | | | | | | |
| Planned Cum. Costs, PC **(baseline)** | **$85,884** | $159,893 | $233,902 | $307,911 | $381,920 | $455,929 | | | |
| | | | | | | | | | |
| Actual Cum. Costs, AC | $11,875 | $11,875 | $41,205 | $149,162 | $149,162 | $455,635 | | | |
| | | | | | | | | | |
| Cost Variance, CV = PC-AC | $74,009 | $148,018 | $192,697 | $158,749 | $232,758 | $294 | | | |

Note 1. Figures shown for Cum. Obligated by DOE match amounts already awarded in grant agreement by quarter end.
Note 2. Planned cost baseline shown accounts for all DOE funding currently awarded.
Note 3. Entries in the row for actual costs shown for future dates are only current estimates of future actual costs, and may be revised later.
Note 4. See report narrative for discussion of any variances.

Attachment 2a

QPR SUMMARY; 9 QUESTIONS & ANSWERS

Grant No. DE-FG02-ER64723
Report Period from 01/01/12 to 03/31/12

Please reply to each of the 9 questions below. (save an unfilled copy for future quarters.)*****
Answers to these 9 questions provide a brief summary of progress and are one part of the Quarterly Progress Report (QPR).

1. Is the project on schedule? Are milestones and other specific schedule items being met? (An up-to-date project milestone log is necessary. It should be included in your full technical QPR.)

**Purchase Completed**

2. Have there been any significant project changes made or requested, (i.e., planned or unplanned changes in project baselines of funding, scope, schedule, costs, design, procurements, subcontracts, or risks, etc.?) Say yes or say no, and if yes then briefly identify them here and cite a reference to the details in the narrative part.

**No other significant changes to the project required**

3. Are DOE funds being expended commensurate with work progress? (Say **Yes**, or No. If no, then explain.)

**Yes, DOE funds ARE expended commensurate with the work completed**.

4. Are project expenditures of DOE funds invoiced to DOE routinely? (Say **Yes**, or No. If no, then explain.)

**Yes, project expenditures of DOE funds are invoiced to DOE by the Office of Sponsored Research**

5. Approximately what are the following cost amounts currently, (in terms of federal DOE funds by *31 Mar.*)*:

Planned-expended: **$455,929** Actual-expended: **$455,635** Invoiced: **$294**

6. How often is project progress and status routinely reviewed internally (by those managing this project)?

**Not Applicable**

7. Do you now expect to transmit the next required written technical QPR on this project up-to-date and on time (i.e., within 30 days following the end of the report period? If not, then very briefly explain the reason.)

**Not Applicable**

8. Overall, in your view, is the project now progressing satisfactorily and expected to be completed as planned, or are there any grant revisions expected to be needed? (e.g., grant expiration date, or other provisions)

**Project completed**

9. Are there any other project issues or comments that you feel should be mentioned here? (Please say yes or say no, and if yes then briefly identify them here, or on added sheets as needed.)

## Project completed

***** Please insert a brief reply in the space following each question. Minimally, say yes or no to questions 1-3 and 7-9. Answer through last day of report period, (e.g. 31 Dec. or other date).Space-sizes provided above are intended to limit the amount of detail usually expected in replies. Add more if you wish. (This is a MICROSOFT WORD file and you can easily insert more text/space as desired. Discuss details if you wish.) My e-mail is edward.gallagher@ch.doe.gov and phone numbers are: voice 630 252 2227 and fax 630 252 2654. (If you respond via fax, then please mark on top/front "To Ed Gallagher", and if you prefer you can print your replies legibly by hand.) My postal address is Edward Gallagher, U.S. Department of Energy Chicago Office 9800 S. Cass Avenue Argonne, IL 60439. In the blank spaces below please give the name, phone number, and e-mail address of the person(s) there for any further discussion of these 9 questions/answers. Thanks for your reply.

Name: ……Mark Kramer ...., phone: …919-966-2629…....., and e-mail: …mkramer@med.unc.edu……...

Grant No. DE-FG02-ER64723

**UNC-Chapel Hill/UNC-Charlotte University Collaborative Initiative in Biomedical Imaging to Study Complex Diseases**

Final report : April 30th 2012

Submitted by Subcontractor: UNC Charlotte

**We report the following:**

1 Fluorescence imaging (Dr. Moyer)

We demonstrate that CdSe/CdS core-shell quantum dots exhibit fluorescence intermittency that is correlated at distances up to one micrometer using a novel fast scan confocal microscopy technique. We perform fast and slow scanning studies that suggest the effect is due to multiple charging of the quantum dots. We provide a quantitative analysis that indicates quantum dots are likely to remain in an emissive state despite taking on multiple charges. This observation contrasts with prevalent blinking models that account only for single charges on quantum dots.

It is well established that quantum dots (QDs) are excellent fluorescent probes due to their robustness, tunable emission, and high level of brightness.[1, 2] Fluorescence blinking is a common phenomenon, but quantum dots are especially well known for their anomalous blinking behavior that follows power-law statistics.[3, 4] Unfortunately, this behavior often negatively impacts the brightness and reliability of QDs for labeling applications.[3] Some research groups have successfully reduced blinking by surface functionalization with organic ligands[5, 6], while others have completely eliminated blinking by synthesizing QDs with novel physical characteristics.[7, 8] Several models have been formulated to explain QD blinking, but none fully capture the breadth of experimental results[9] and questions regarding the mechanism of fluorescence intermittency remain unanswered.

Using a confocal microscopy method that we call fast-scanning confocal microscopy (FSCM), we have observed that two QDs in close proximity to each other (<1 μm) exhibit fluorescence trajectories that are correlated. The strength of this blinking correlation is inversely proportional to the distance between the respective QDs, suggesting the existence of an inter-QD coupling mechanism via long-range electrostatic interactions. We demonstrate that this correlated blinking is most likely caused by the photo-generation of highly charged QDs. Our data suggests that the amount of photo-generated charge that builds up on QDs exceeds the levels theorized in recent "multiple charging" models.[10] The charged QDs produce an electric field effect capable of modulating the fluorescence trajectories of neighboring QDs.

FSCM takes advantage of the typically inconvenient limit of scanning confocal microscopy, serial imaging. Instead of building a complete two-dimensional image with each series of scans, we instead limit the fast scan direction of the stage to a single dimension. In other words, the

slow scanning axis is fixed at a negligible scan distance (Figure 1b) and the gathered image is simply a distance vs. time plot (Figure 1c). This technique allows us to monitor the fluorescence trajectories of two or more nearby particles in a singe experiment.

As illustrated in Figure 1c, three QDs display the expected blinking dynamics with probability densities that obey power law statistics typical of nanocrystal fluorescence.[11, 12] Blinking models attempt to account for this in a number of ways, but to date no single model fully explains the behavior while maintaining consistency with experimental data. Our findings suggest that neighboring QDs influence QD fluorescence trajectories and, therefore, a full theoretical treatment of QD blinking should be able to account for these interactions.

Our homebuilt laser scanning confocal microscope utilizes a 470 nm diode, 300 picosecond pulse laser.[13] Using a 10 Mhz pulse rate, the average irradiance for these experiments was 2.5 $kW \cdot cm^{-2}$. The excitation beam was coupled into a single mode optical fiber and subsequently passed through a 470/20 nm band-pass filter (BPF). The excitation beam was subsequently reflected from a 500 nm dichroic beam splitter (DBS) into a 1.25 N.A. 100x oil-immersion objective lens, which also served as the collection lens for the fluorescent light. The DBS passed all wavelengths above 500 nm, after which a second DBS, at 585 nm, was used to split the emission signal for two-color imaging. Finally, a 565/40 nm BPF and a 605/52 nm BPF were used in front of two separate MPD-series single photon avalanche diodes.

Figure 2 shows that, especially at distances <1μm, pairwise QD fluorescence correlation is consistently greater that one standard deviation from the mean random correlation. There is clearly a statistical significance to the distance dependent blinking correlation of adjacent QDs and we can therefore conclude that at distances of up to ~1μm, neighboring QDs affect the blinking behavior of each other. This long distance correlation is quite remarkable considering that the characteristic distances of charge transfer and electron transfer are one or two orders of magnitude smaller than this.

We suspect that particle charging effects as act as the primary cause of the correlation observed, and we will provide evidence that QDs routinely become charged at up to about +/- 5 $e^-$ while still likely remaining in an on state. This effect can be summarized by a basic consideration of a Coulomb interaction between point charges, $U = N_1 N_2 q_1 q_2 / 4\pi\varepsilon\varepsilon_0 R$, where $N_1$ and $N_2$ are the number of charges on dot 1 and dot 2 respectively and R is the distance between correlated quantum dots. Putting a single charge on each QD, $N_{1,2}=1$, ($q=1.602 \times 10^{-19}$ C, $\varepsilon_0=8.854 \times 10^{-12}$) in the presence of a PMMA matrix of static dielectric constant (ε) 3.5, the magnitude of the potential energy, U, is 0.822 meV for a 500 nm dot separation. Based on the low temperature results of Neuhauser et al. in which they indicate a correlation between blinking and spectral diffusion of individual quantum dots of up to 45 meV, we are highly skeptical of 0.822 meV being large enough to cause a perturbation significant enough to measure a statistical correlation in blinking behavior. We do note, however, that our method introduced in this paper of observing and characterizing statistical correlation in fluorescence intermittency is very sensitive to very small effects on adjacent QDs but 0.822 meV seems too small at a relatively large distance of 500 nm. Consider further that we can measure a correlation for dots up to 1000 nm apart and a perturbation of 0.411 meV is even more unlikely to have a noticeable effect.

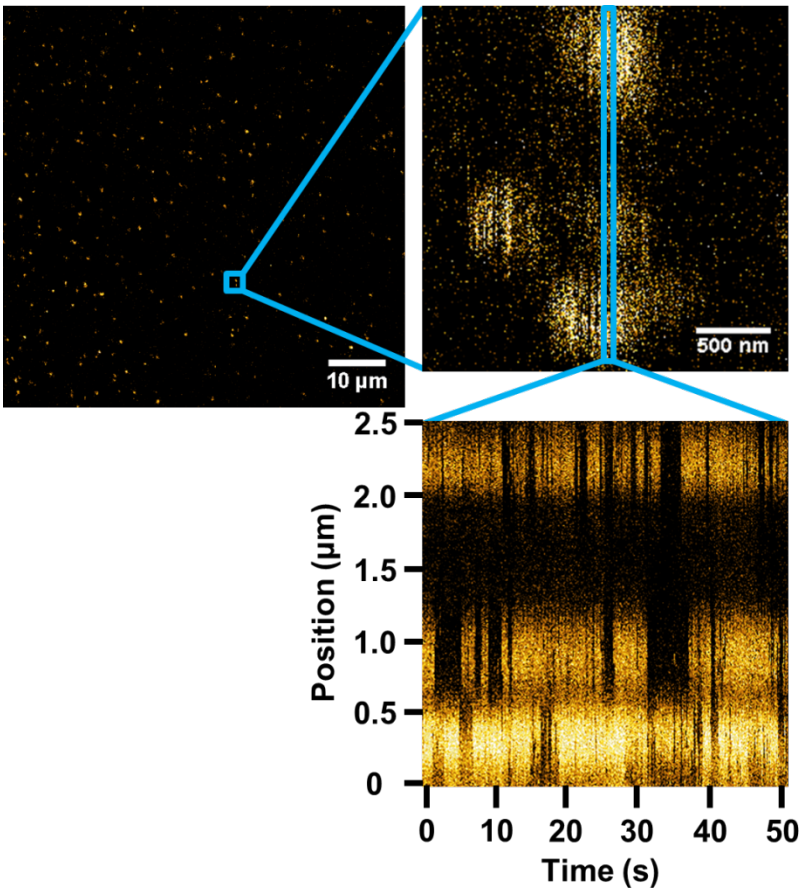


**Figure 1.** (a) 70 x 70 µm image of 5 x $10^{-11}$ M quantum dots spin coated onto glass in poly(methyl methacrylate). (b) Zoomed image to 2.5 x 2.5 µm area showcasing four single quantum dots with their characteristic blinking. (c) Position vs. time trace for highlighted area from 1b. The blinking pattern for three QDs can be easily identified.

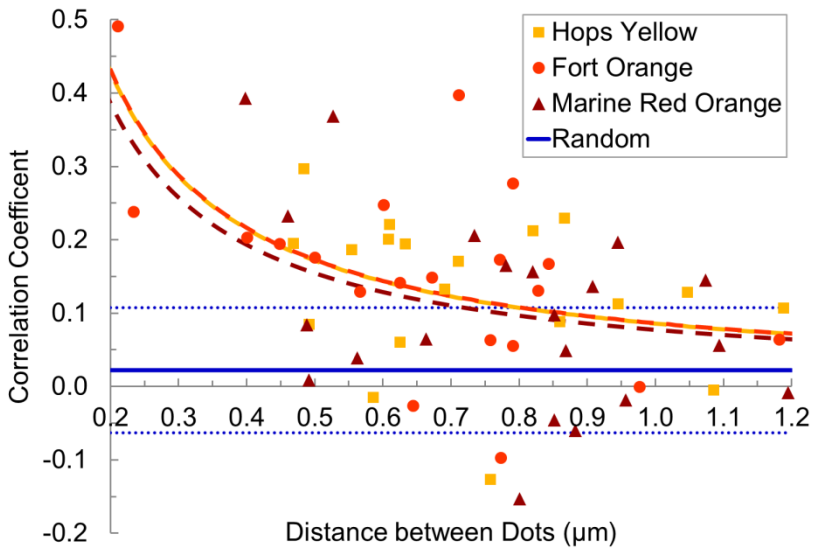


**Figure 2.** Three types of Evidots are plotted by distance between neighboring dots and calculated correlation coefficient. A random pairing of data sets from the Evidots was used to generate the random set of data shown. The dotted lines represent one standard deviation for the random pairings. Note that each set of data is fit to a 1/R relationship (R=distance between quantum dots).

**References**


1.Alivisatos, A. P. Science **1996,** 271, (5251), 933-937.
2.Murray, C. B.; Norris, D. J.; Bawendi, M. G. Journal of the American Chemical Society **1993,** 115, (19), 8706-8715.
3.Nirmal, M.; Dabbousi, B. O.; Bawendi, M. G.; Macklin, J. J.; Trautman, J. K.; Harris, T. D.; Brus, L. E. Nature **1996,** 383, (6603), 802-804.
4. Banin, U.; Bruchez, M.; Alivisatos, A. P.; Ha, T.; Weiss, S.; Chemla, D. S. Journal of Chemical Physics **1999,** 110, (2), 1195-1201.
5.Early, K. T.; McCarthy, K. D.; Hammer, N. I.; Odoi, M. Y.; Tangirala, R.; Emrick, T.; Barnes, M. D. Nanotechnology **2007,** 18, (42), 7.
6.Hohng, S.; Ha, T. Journal of the American Chemical Society **2004,** 126, (5), 1324-1325.
7.Mahler, B.; Spinicelli, P.; Buil, S.; Quelin, X.; Hermier, J. P.; Dubertret, B. Nature Materials **2008,** 7, (8), 659-664.
8.Chen, Y.; Vela, J.; Htoon, H.; Casson, J. L.; Werder, D. J.; Bussian, D. A.; Klimov, V. I.; Hollingsworth, J. A. Journal of the American Chemical Society **2008,** 130, (15), 5026-5027.
9.Frantsuzov, P.; Kuno, M.; Janko, B.; Marcus, R. A. Nature Physics **2008,** 4, (7), 519-522.
10. Califano, M. Journal of Physical Chemistry C **2011,** 115, (37), 18051-18054.

## 2 Optical coherence tomography (Dr. Fried)

### Summary

One of the greatest challenges of prostate cancer surgery is preservation of sexual function after surgery. There is wide variability in reported post-operative potency rates (9 - 86%). This variability may be due, in part, to our limited understanding of the location, extent, and course of the cavernous nerves, which are responsible for erectile function. Because of the close proximity of the nerves to the surface of the prostate, they are at risk of damage during surgical dissection and removal of a cancerous prostate gland. In addition, their microscopic nature makes it difficult to predict the true course and location of these nerves from one individual patient to another. Improvements in identification, imaging, and visualization of these nerves will likely improve the consistency of nerve preservation and postoperative potency, leading to an improved quality of life for patients. We tested two complementary optical technologies: laser stimulation for identification of the cavernous nerves, and high-resolution optical coherence tomography (OCT) for imaging of cavernous nerves.

### Key Accomplishments

- We optimized the laser parameters to produce the strongest and most rapid erectile response as measured by intracavernosal pressure (ICP) in the penis. ICP values were increased from an initial range of 30-40 mmHg during preliminary studies to a range of 50-60 mmHg. The optimal laser stimulation parameters were observed at wavelengths of 1860-1870 nm, pulse energies of 2.7–8.0 mJ (0.35-1.0 J/cm$^2$), and a pulse rate of 10 Hz. Lower pulse energies and pulse rates failed to produce an ICP response during 60 s stimulation, while higher pulse energies and pulse rates resulted in thermal damage to nerve and loss of nerve function.

- Direct comparative studies between laser nerve stimulation and electrical nerve stimulation were performed, demonstrating no significant difference in peak ICP between the two techniques.

- A compact, laparoscopic laser nerve stimulation probe was designed for use in preclinical and clinical studies. The handheld, side-firing probe is capable of rapid scanning of a laser beam across the surface of the prostate with a laser power density sufficient for nerve stimulation. The probe fits through a standard, 5-mm-OD laparoscopic port typically used in the clinic for laparoscopic and robotic prostate cancer surgery.

- Computer image processing algorithms were applied to optical coherence tomographic (OCT) images of the rat cavernous nerves and the prostate to de-noise the images and make it easier for a clinician to differentiate between the cavernous nerves and the prostate during prostate cancer surgery. A signal-to-noise (SNR) increase of 14 dB was achieved using these algorithms.
- A laparoscopic laser nerve stimulation probe was designed incorporating both laser beam collimation and beam shaping. The probe produced a collimated 1-mm-diameter spot over a working range of 20 mm. The standard Gaussian laser beam shape was also converted into a flat-top beam profile, providing more uniform irradiation of the cavernous nerve surface during stimulation. These features are significant because application of laser nerve stimulation as an

intra-operative diagnostic tool during prostate cancer surgery will require delivery of a constant energy density to the nerve. Too low an energy will result in no stimulation and too high an energy will result in thermal damage to the nerve and consequent loss of erectile function. Our handheld laparoscopic probe produces a range of working distances providing constant and reproducible nerve stimulation.

- We have discovered that the threshold for laser stimulation of nerves is significantly lower than previously reported. Our research group working on the rat cavernous nerve model, as well as other research groups working on other peripheral nerve models, previously reported the threshold radiant exposure for laser nerve stimulation to be about 0.35 J/cm$^2$. However, using our improved flat-top laser nerve stimulation probe, we recorded successful cavernous nerve stimulation at laser radiant exposures of only 0.14 J/cm$^2$. This result is significant because use of a lower energy provides less probability of thermal damage to the nerve during stimulation, and also potential for use of a less expensive laser during clinical application. The flat-top probe provides much easier alignment of the laser spot with the nerve, thus producing more reliable stimulation at lower radiant exposures.

- Using our improved flat-top laparoscopic probe, we have also managed to reduce the stimulation time from 30-60 s recorded during previous studies, to less than 10 s reported during our current studies. This is significant because stimulation has to be fast and close to real-time feedback provided for the technique to be clinically viable.

- The optical properties of the prostate gland were measured for the first time at near-infrared laser wavelengths (l = 1064, 1310, and 1550 nm) for potential use with OCT systems. Our study found improved optical penetration depth at 1064 nm in comparison with the conventional 1310 nm wavelength currently used in OCT. This is significant because the greatest limitation to clinical application of OCT prostate imaging is the limited imaging depth.

- We applied an image processing technique, known as segmentation, to OCT images of rat cavernous nerves and prostate, providing enhanced contrast between the two structures. We have also added edge detection to our denoising and segmentation algorithms to effectively provide deeper prostate imaging, with an improvement from ~ 1-mm depth to ~ 1.6-mm depth.

- Two different OCT systems (time-domain and Fourier-domain) were compared using image metrics (SNR, CNR, and equivalent number of looks). Although the TD-OCT system has a slower image acquisition time, it had superior signal-to-noise ratio for deeper imaging of the prostate gland.

- A continuous-wave (CW) method of optically stimulating the prostate nerves was developed, resulting in faster stimulation of nerves at relatively low stimulation thresholds of 50 mW at 1870 nm.

- An alternative diode laser wavelength (l = 1455 nm) was used for optical stimulation of the cavernous nerves which is more compact and less expensive than the Thulium fiber laser (l =

1870 nm) used in previous studies. This laser wavelength was also more efficiently absorbed by the nerves, resulting in an even lower stimulation threshold of only about 30 mW.

- An all-single-mode optical fiber based optical nerve stimulation system was built and tested using the 1455 nm diode laser, and Gaussian and flat-top spatial beam profiles were compared for fast stimulation of the prostate nerves. The stimulation time was further reduced from 30-60 s in Year 1 studies to approximately 9 s in Year 2 studies, to about 3-4 s using this system in Year 3 studies.

- Successful "subsurface" optical stimulation of the prostate nerves was achieved by transplanting a layer of fascia over the rat prostate nerve. A 1550 nm laser was used for deeper penetration of the laser energy through the fascia, and we demonstrated successful subsurface stimulation through fascia layers up to 450 mm thick, greater than the typical 100-300 mm fascia layer in the human.

**Peer-Reviewed Manuscripts**


1. Chitchian S, Fiddy MA, **Fried NM**. Denoising during optical coherence tomography of the prostate nerves via wavelet shrinkage using dual-tree complex wavelet transform. Journal of Biomedical Optics 14(1):014031, 2009.

2. Chitchian S, Weldon TP, **Fried NM**. Segmentation of optical coherence tomography images for differentiation of the cavernous nerves from the prostate gland. Journal of Biomedical Optics 14(4):044033, 2009.

3. Tozburun S, Lagoda GA, Mayeh M, Farahi F, Burnett AL, **Fried NM**. A compact laparoscopic probe for optical stimulation of the prostate nerves. IEEE Journal of Selected Topics in Quantum Electronics 16(4):941-945, 2010.

4. Tozburun S, Cilip CM, Lagoda GA, Burnett AL, **Fried NM**. Continuous-wave infrared optical nerve stimulation for potential diagnostic applications. Journal of Biomedical Optics 15(5):055012, 2010.

5. Chitchian S, Weldon TP, Fiddy MA, **Fried NM**. Combined image processing algorithms for improved optical coherence tomography of the prostate nerves. Journal of Biomedical Optics 15(4):046014, 2010.

6. Tozburun S, Lagoda GA, Burnett AL, **Fried NM**. Continuous-wave laser stimulation of the rat prostate cavernous nerves using a compact and inexpensive all single mode optical fiber system. Journal of Endourology 25(11):1727-1731, 2011.

7. Tozburun S, Lagoda GA, Burnett AL, **Fried NM**. Subsurface near-infrared laser stimulation of the periprostatic cavernous nerves. Journal of Biophotonics. In press.

**Peer-Reviewed Conference Proceedings Papers**

1. Tozburun S, **Fried NM**. Design of a compact laparoscopic probe for optical stimulation of the cavernous nerves. Proc. SPIE 7161:13:1-4, 2009.

2. Chitchian S, Fiddy M, **Fried NM**. Speckle reduction during all-fiber common-path optical coherence tomography of the cavernous nerves. Proc. SPIE 7168:2N:1-6, 2009.

3. Chitchian S, Fiddy M, **Fried NM**. Denoising during optical coherence tomography of the prostate nerves via bivariate shrinkage using dual-tree complex wavelet transform. Proc. SPIE 7161:12:1-4, 2009.

4. Chitchian S, **Fried NM**. Near-IR optical properties of canine prostate tissue using oblique-incidence reflectometry. Proc. SPIE 7548: 75480Z:1-6, 2010.

5. Chitchian S, Weldon TP, **Fried NM**. OCT image segmentation of the prostate nerves. Proc. SPIE 7443: 74431D:1-4, 2010.

6. Tozburun S, Lagoda GA, Burnett AL, **Fried NM**. Gaussian versus flat-top spatial beam profiles for optical stimulation of the prostate nerves. Proc. SPIE 7548: 75484W:1-6, 2010.

7. Tozburun S, Lagoda GA, Mayeh M, Burnett AL, Farahi F, **Fried NM**. Incorporation of fiber optic beam shaping into a laparoscopic probe for laser stimulation of the cavernous nerves. Proc. SPIE 7548:754818:1-5, 2010.

8. Chitchian S, **Fried NM**. An edge detection algorithm for improving optical coherence tomography images of the prostate nerves. OSA BIOMED, 2010.

9. Tozburun S, Cilip CM, Lagoda GA, Burnett AL, **Fried NM**. Continuous-wave optical stimulation of the rat prostate nerves using an all-single-mode 1455 nm diode laser and fiber system. Proc. SPIE 7883:788352:1-6, 2011.

10. Chitchian S, Lagoda GA, Burnett AL, **Fried NM**. Fourier-domain versus time-domain optical coherence tomography of the prostate nerves. Proc. SPIE 7883:788314:1-7, 2011.

11. Tozburun S, Lagoda GA, Burnett AL, **Fried NM**. Continuous-wave versus pulsed infrared laser stimulation of the rat prostate cavernous nerves. Proc. SPIE 7883:78831A:1-6, 2011.

12. Tozburun S, Lagoda GA, Burnett AL, Farahi F, **Fried NM**. Fiber beam shaping for optical nerve stimulation. IEEE Photonics Society Annual Meeting (IPC11) WL6:493-494, 2011.

13. Tozburun S, Lagoda GA, Burnett AL, **Fried NM**. Subsurface optical stimulation of the rat prostate nerves using continuous-wave near-infrared laser radiation. Proc SPIE 8207:82070Y:1-6, 2012.

**Abstracts**

1. **Fried NM**, Chitchian S, Tozburun S, Lagoda GA, Burnett AL. Optical coherence tomography and optical nerve stimulation for imaging and identification of the prostate nerves. DOD Innovative Minds in Prostate Cancer Today (IMPaCT) Meeting, Orlando, FL, March 2011.

3 X-ray interferometer/phase imaging system (Dr. Smith)

## Final report of scanned x-ray interferometric phase contrast imaging (SXRPCI) facility

### *Overview*

The goal of this research program was to design, manufacture and commission and function scanned x-ray interferometric phase contrast imaging facility. Figure 1 below shows a schematic diagram indicating key sub-system components of the facility from the original proposal. While being a planned project task in the original proposal, absent from this diagram is the x-ray enclosure and related safety features. Major milestones achieved by this project are;

1. Design and construction of the enclosure for the x-ray facility and noise isolate chamber for the x-ray generator chilled water unit.
2. Purchase of all systems components and testing of software communications.
3. Development of process control architecture for the process.
4. Drafting of a review of x-ray diffraction theory for thick crystals.
5. Funding support for system characterization and calibration over the following two years.

With the exception of the review that is provided in appendix A in this document, a brief overview of these tasks is provided in this report.

### *Design and manufacture of the enclosures for the x-ray facility and water chiller acoustic isolation*

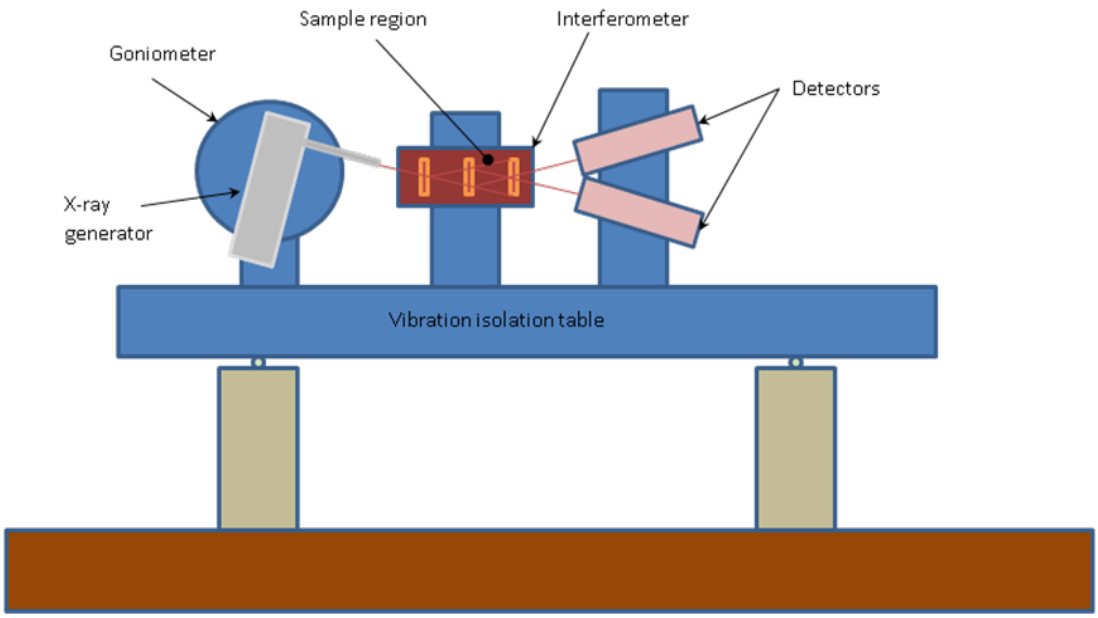


Figure 1: Overview of major components of the SXRPCI system

The enclosure for this system underwent a number of design revisions prior to final detailing of components. Initial designs were for a leaded enclosure surrounding the complete system. After considering the logistics of implementing such a construction, it was decided to produce an enclosure to be mounted onto the vibration isolation table itself. A solid model of this is shown in Figure 2. To make this system relatively portable, considerable effort was invested in the assembly of this enclosure from modular parts. Some of the relevant design features for this are shown in Figure 3. To provide clearance for a labyrinth of lead sheet it was necessary to incorporate sufficient space in all components of the assembly. A photograph of the enclosure at an earlier stage of development is shown in Figure 4. Controller hardware is also shown on top of the enclosure.

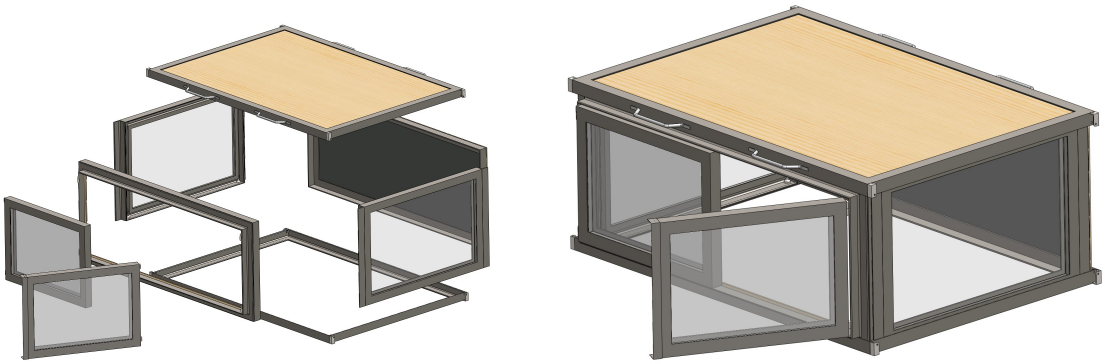

Figure 2: Exploded view of modular components of the enclosure (left), solid model of assembled enclosure

Finally, there were some concerns about the noise from the chilled water supply being

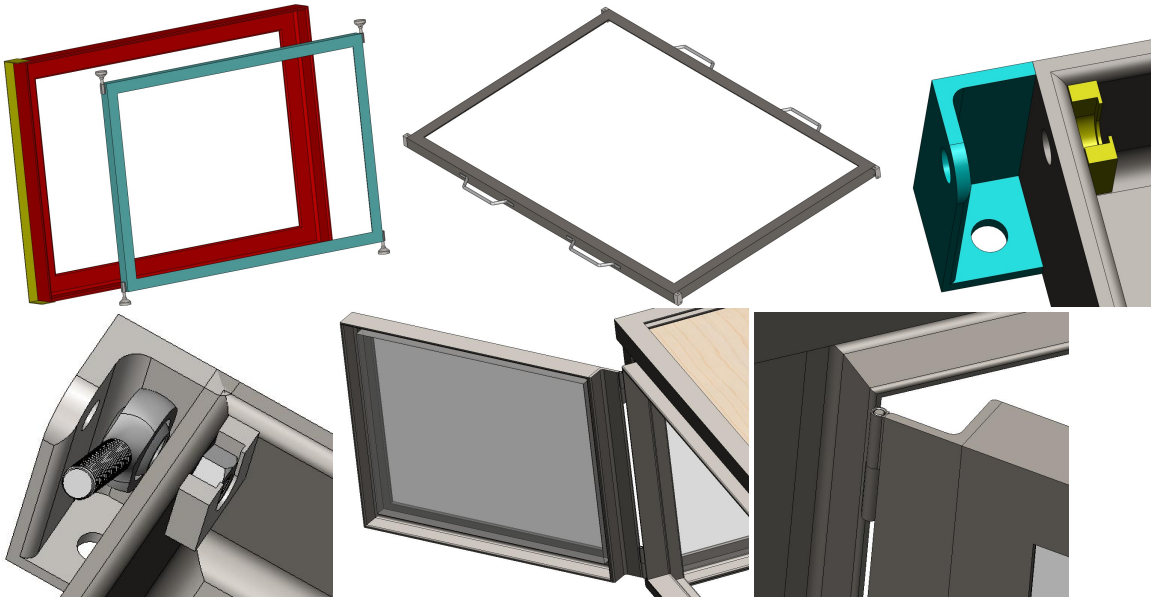

Figure 3: Detailed design features for the modular components of the enclosure assembly.

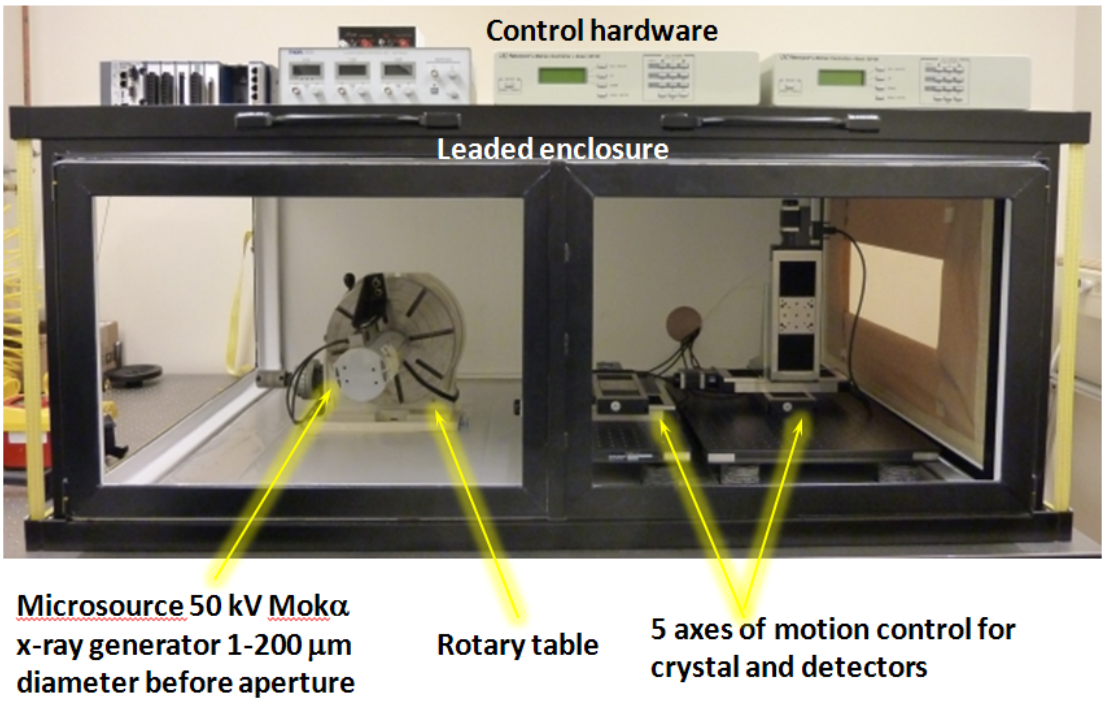


Figure 4: Photograph showing major components of the enclosure assembly and interferometer subsystems.

transmitted into the interferometer crystal. In an effort to attenuate acoustical sources an acoustic chamber was also designed, see Figure 5, and this will be housed outside of the laboratory with chilled water feed tubes going through holes in the wall.

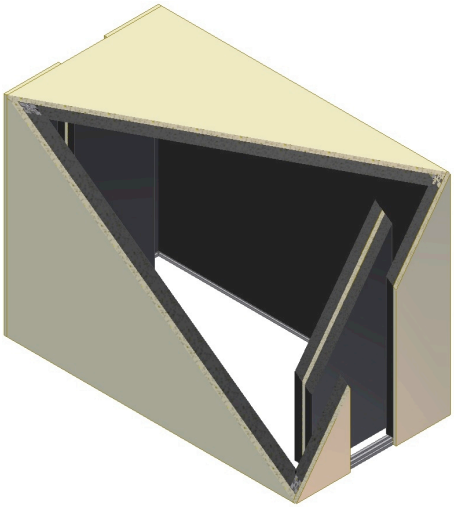

Figure 5: Solid model of acoustical chamber showing labyrinth path for air cooling.

### *Purchase of systems components and development of controller architecture*

Systems components such as the micro-source x-ray generator, specimen $xy$ positioner and materials for construction of the apparatus were purchased throughout the project. Purchase of translation stages for positioning and alignment and controllers were delayed pending completion of the enclosure that occurred in the final six month period of this project.

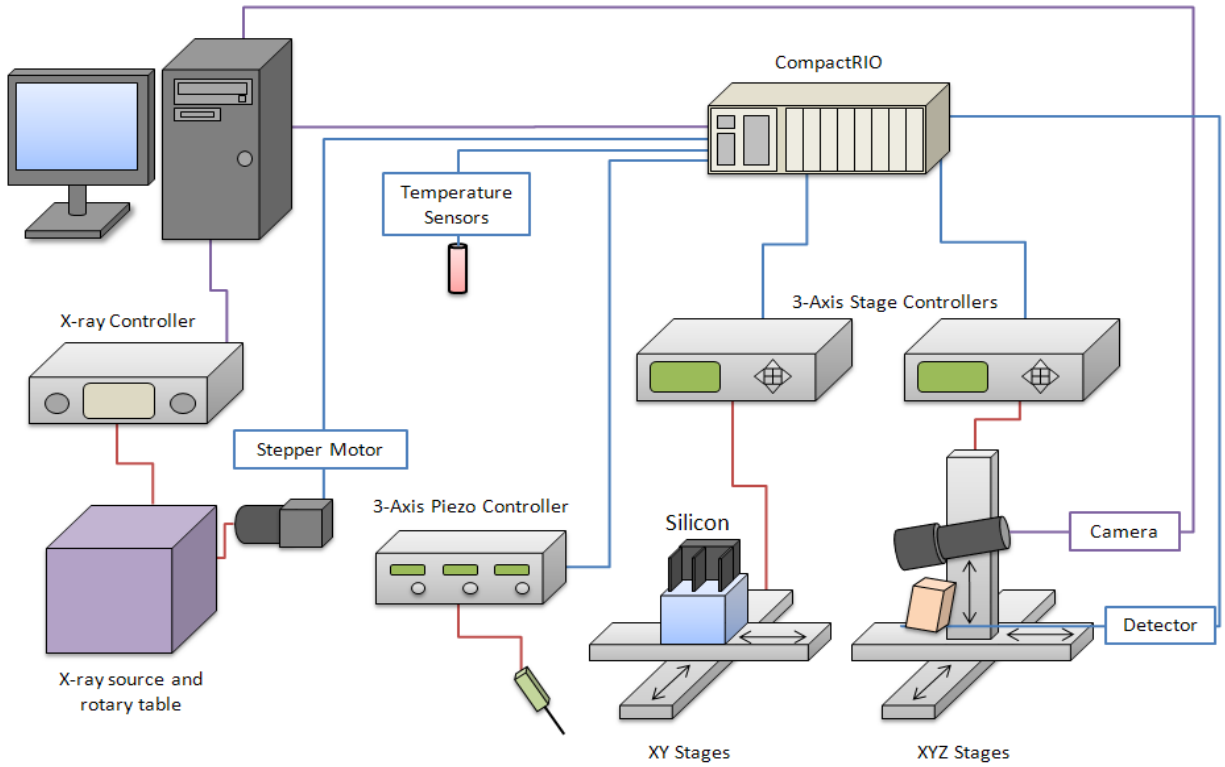


Figure 6: Block diagram showing major components of the controller for the facility (for clarity the specimen positioner is not shown).

A controller block diagram is shown in Figure 6. The piezo-electric actuator of this system is to be used to provide translation of the analyzer blade of the interferometer to provide phase shifting interferometry. To obtain controllable displacements at fractions of the (220) lattice spacing, a thin fiber of high compliance will be used to apply a force to the stiff flexure that supports the analyzer crystal. Continuous control of all sub-systems will be achieved using the compact Real-time Input/Output (cRIO) chassis that can be individually programmed into its FPGA. As a consequence, the central host computer will operate primarily as a supervisor sending high level instructions to the controller through an Ethernet bus.
As of writing all of these sub-system components have been controlled using interface software generated using the Labview™ development environment.

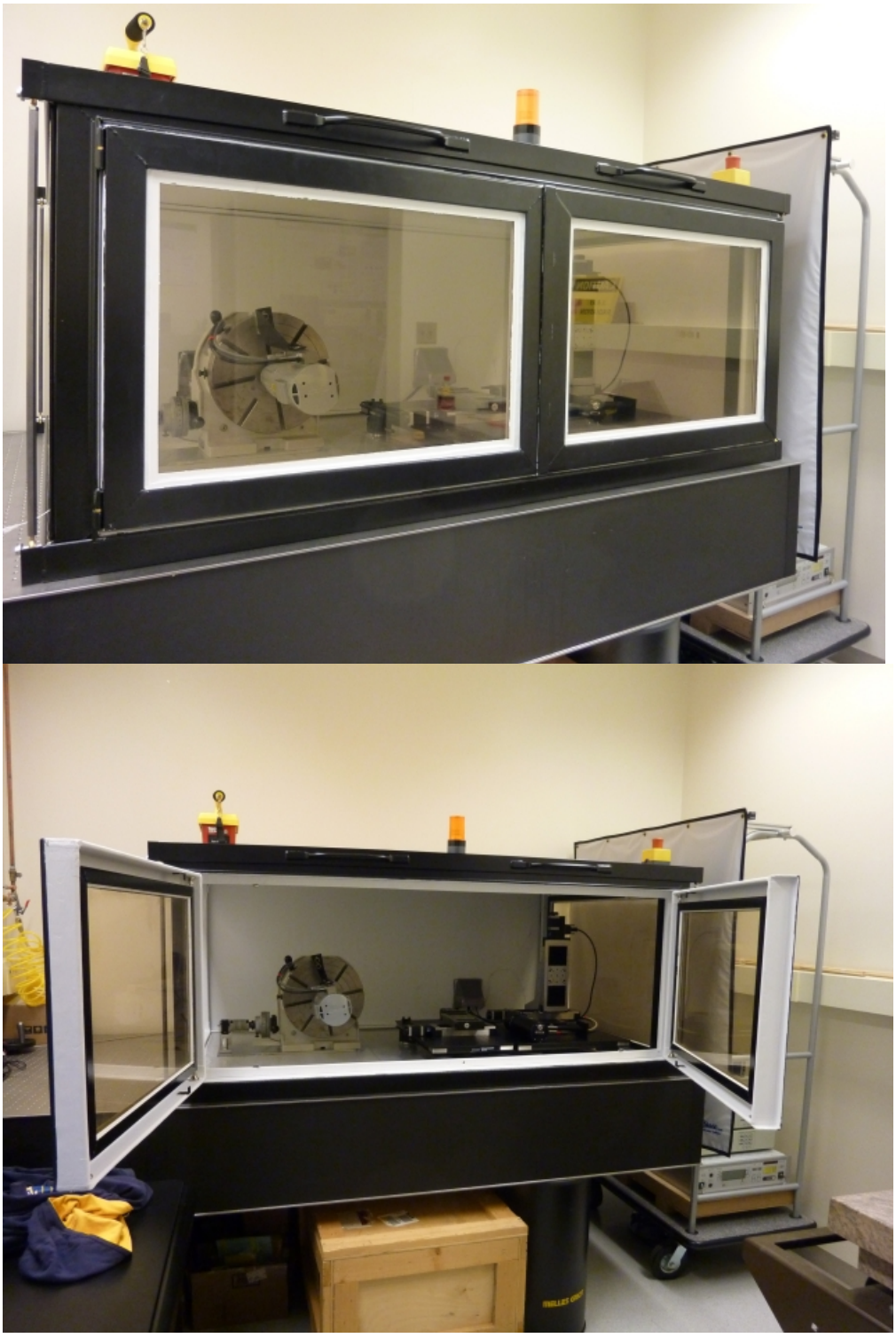

Figure 7: Photograph of x-ray interferometer facility with access dors shut (top photograph) and open (lower photograph).

Being the only phase mapping initiative in the US outside of synchrotron facilities (some work

on this was recently reported from Japan), it is expected that results produced from this project will be complimentary to the micro CT research that is actively being developed around the world and of interest to the scientific community.

### *References relevant to modeling of x-ray interferometer optics*


Hart, M., An angstrom ruler, *Brit. J. Appl. Phys.* (*J. Phys. D*), Ser. 2, **1**, 1405 (1968)
Bonse, U. and M. Hart, Principles and design of Laue-case x-ray interferometers, *Z. Physik*, **188**, 154 (1965)
Bonse, U. and M. Hart, *Z. Physik*, **190**, 455 (1966)
B. L. Henke, E. M. Gullikson, and J. C. Davis, "X-Ray Interactions: Photoabsorption, Scattering, Transmission, and Reflection at $E$ = 50–30,000 eV, $Z$ = 1–92," *At. Data Nucl. Data Tables* **54,** 181 (1993).
Hecht, E., *Optics*, Addison-Wesley Pub. Co., Reading, Mass., 1987
Goodman, J. W., *Introduction to Fourier Optics*, McGraw Hill, New York, 1968
James, R. W., *The Optical Principles of the Diffraction of X-Rays*, Ox Bow Press, Woodbridge, Conn., 1962
H Kuwabara, W Yashiro, S Harasse, H Mizutani, and A Momose, Hard-X-ray Phase-Difference Microscopy with a Low-Brilliance Laboratory X-ray Source Published June 13, 2011 (3 pages)
Warren, B. E., *X-Ray Diffraction*, Dover Publications, New York, 1990
Batterman, B. W. and H. Cole, *Rev. Mod. Phys*., **36**, 681 (1964)
Papoulis, A., *Signal Analysis*, McGraw Hill, New York, 1977

## Appendix A: Theoretical aspects of x-ray diffraction for thick crystals

***Theoretical development of the propagation of x-rays through an interferometer***

***John Carter, Stuart T. Smith, Jeffrey Thousand***

***Introduction and kinematical diffraction***

The interferometer orientation used in our work corresponds to the x-ray beam being launched into thick parallel crystals diffracted in the 220 plane that is parallel to the normal of the crystal surface. Silicon is a diamond cubic crystal, see Figure 3 with lattice parameters given in Table 1. Each unit cell is essentially a face centered cubic crystal (containing 4 atoms) with a further four atoms located at positions ¼ of a lattice spacing inside the unit cell from each corner. This

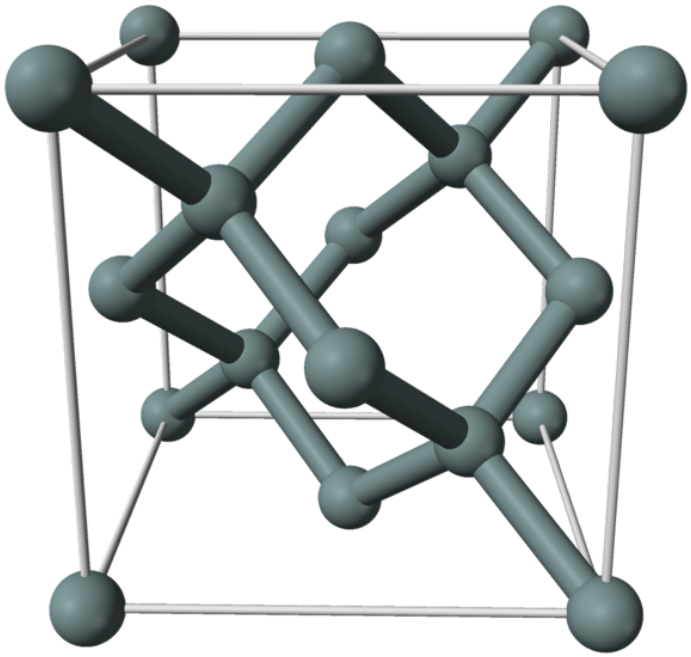

Figure 2: Three dimensional model of silicon lattice (from Wikipedia)

can also be built up from tetrahedral units all having similar orientation.

Table 1: Silicon lattice parameters

| Lattice parameter[1] | Dimension (nm) |
|---|---|
| $a$ | 0.54310204 (±3) |
| $d_{220}$ | 0.192015569 |
| $V$ | 0.16019 ($nm^3$) |

The theoretical foundation of interferometry takes the form of extending formal x-ray theory for the case of dual inputs near to the Bragg angle and the subsequent energy transfer normal to the reciprocal lattice and therefore along the diffraction planes. This is commonly referred to as the Borrmann effect and considerably complicates analysis. Following the energy flow through the crystal, it is then necessary to compute the emergent x-rays from the crystal. As a precursor to this, it is necessary to review the basis of diffraction in periodic potentials. Figure 1 shows the usual kinematic view of diffraction using the Ewald construction governing the conditions for diffraction. Two spaces have been superposed in this figure. In the background is the actual crystal lattice modeled as ideal planes with lattice separation denoted $h_{jkl}$. A vector shows the x-ray beam incident on the surface. On top of this figure is the reciprocal lattice indicating one lattice point that represents all planes in subsequent analysis. In this 2-D representation, the circle represents a sphere of radius $1/\lambda$, where $\lambda$ is the wavelength of incident radiation. A vector $\overrightarrow{K_0}$ is drawn from the center of the sphere (later to be called the Lorentz point $L_o$) to the origin of the reciprocal lattice space. As drawn, this sphere also passes through the reciprocal lattice point. From the kinematical theory of x-ray diffraction this geometry represents Braggs condition for diffraction in a generalized form in which the refractive index is assumed unchanged for x-rays in air and while being diffracted in the crystal. This means that the angle of incident and refracted waves within the crystal are, incorrectly, all at the same angle, a feature to be cleared up with the development of the dynamical theory. In this representation, the crystal lattice is assumed to be an idealized scattering plane. Therefore this diagram can be considered to represent geometrically, the wave vectors of the incident x-ray beam and emergent x-ray beams. Such an idealized model ignores the wavefields generated during propagation in a real crystal for which a more complete model given by dynamical diffraction is required. The wave vectors in Figure 3 and Figure 4 represent the incident and emergent beams based on the idealized geometric diffraction model.

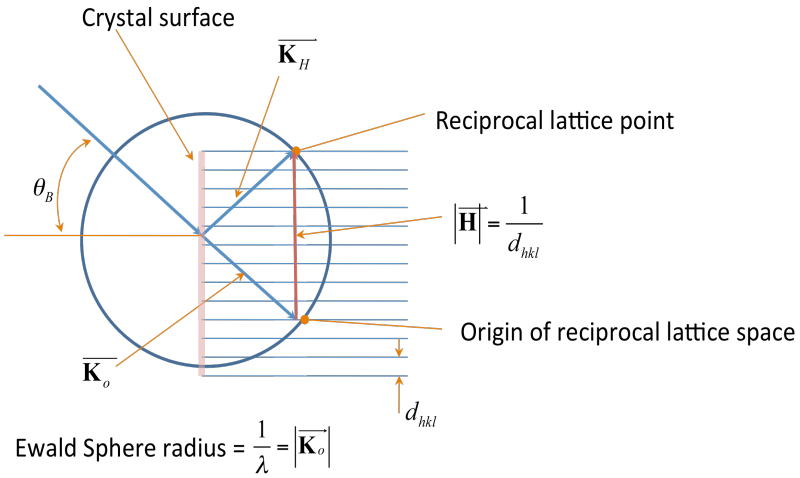


Figure 3: Geometric model representing conditions for diffraction in a perfect crystal.

Given that the condition shown in Figure 3 applies to a system model, it is possible to drawn this in the alternative form shown in Figure 4. It can now be observed that the incident beam points to the intersection of the two Ewald spheres now centered around the reciprocal lattice point and reciprocal space origin.

It is now observed in Figure 4 that the incident beam points to the intersection of the two Ewald spheres now centered at the reciprocal lattice point and reciprocal space origins respectively. In practice, polarization, crystallographic structure, electron charge distributions and interrelated index of refraction variations will influence this diffraction condition resulting in a broadening of the array of spheres that satisfy the diffraction condition. However, it is still possible to use the Ewald construction extending the number of possible sphere originating from a surface points called the dispersion surface. To see this it is necessary to zoom in on the region in the vicinity of the $Q$ point. This has been reproduced from Batterman and Cole . In this diagram there is a new Ewald sphere at origin $L$ plus others originating from so called tie points on the dispersion surface.

For the purpose of this review we will develop the equations relating dispersion surface diagrams of relevance to the Laue mode operation of a three crystal interferometer. For modeling purposes this configuration for a perfect system is of the form shown in Figure 5. Detailed models necessary to understand the physical process of the interferometer must include the one wave transmission including the Borrmann effect and the subsequent propagation through both the splitter and mirror blades followed by the 2 wave modeling of the analyzer blade action.

The two wave action must be modeled in terms of the spatial phase of the lattice in conjunction with two incident beams as they converge from the mirror blade of the interferometer, see Figure 6. Analysis based on the equations derived from modeling of equations governing the processes shown in figures 1 through 3 can then be applied to determine the characteristics of the emergent beams from the analyzer blade. It is envisaged that this model will be expandable to investigate crystal imperfections and manufacturing tolerance effects of relevance to manufacture of interferometer system of differing sizes and geometric (i.e. Bragg and Laue) configurations.

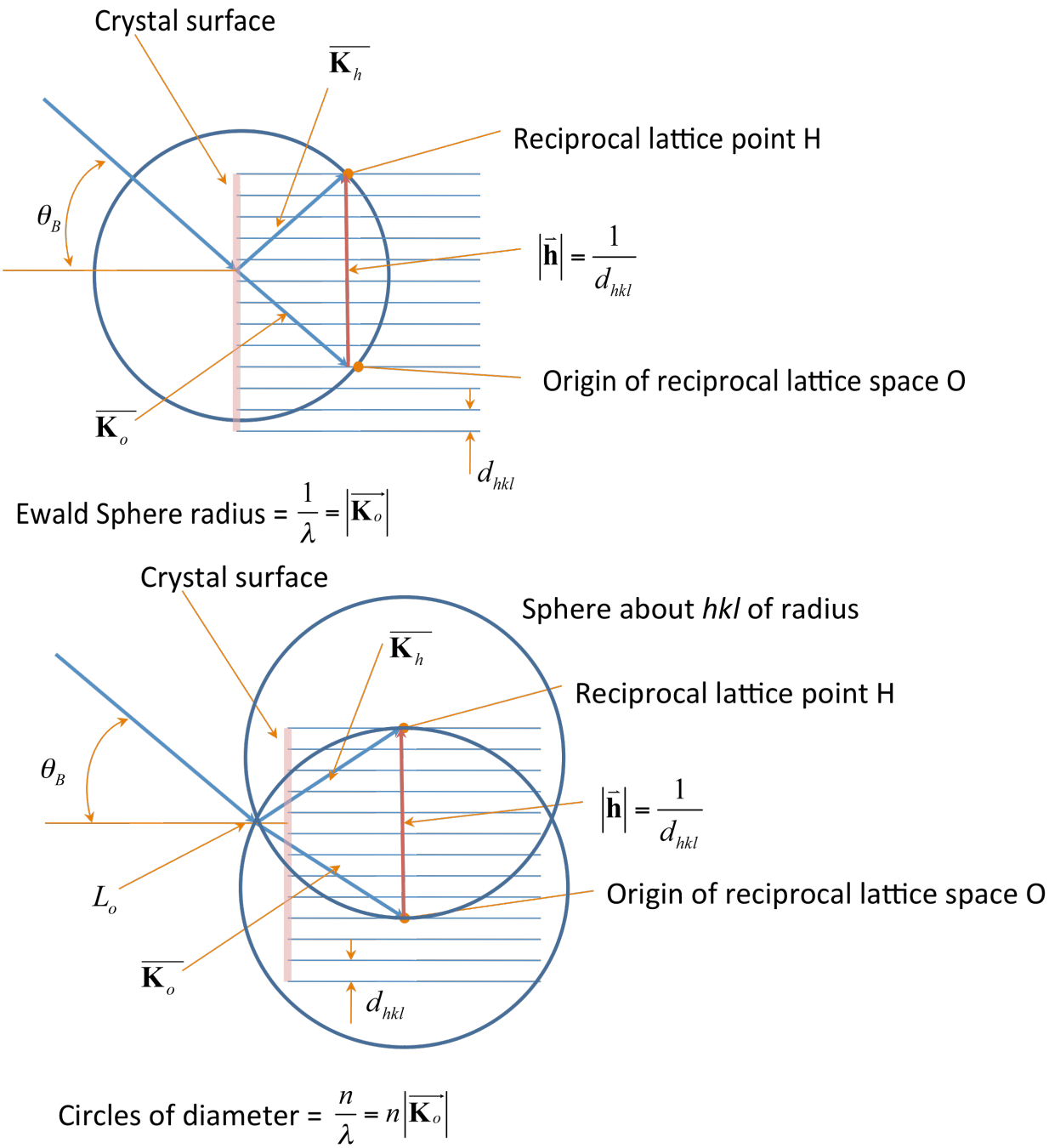


Figure 4: Equivalent geometry given that Ewald diffraction condition is satisfied in the simple kinematic theory. Crystal lattice in real space also show for diffraction planes normal to crystal surface, a) loci of permitted Ewald spheres with original kinematical sphere shown (not being a permitted solution), b) Two circles with wave vector radius scaled by the refractive index and centered on reciprocal lattice points $O$ and $H$.

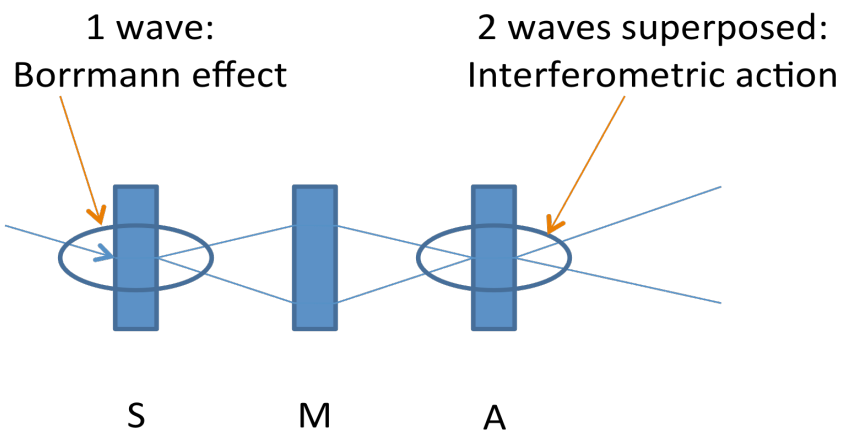


Figure 5: Ideal x-ray interferometer system

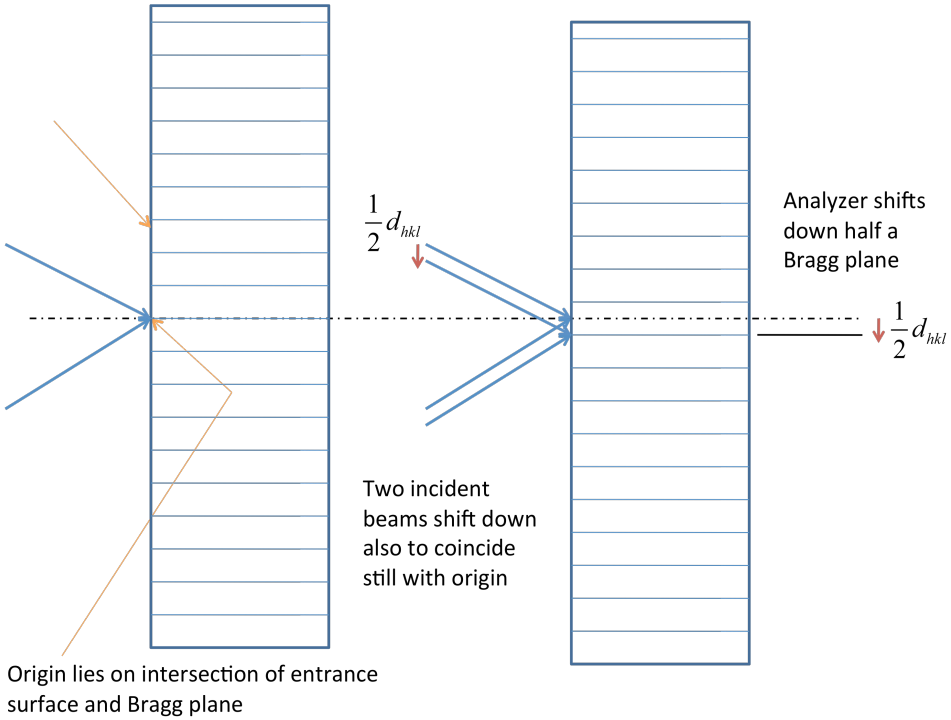


Figure 6: Details of two x-ray beams converging on the surface of the analyzer blade.

## *Real crystal diffraction in Silicon*

Waves propagating in an infinite crystal have a reflection domain consisting of an ideal point. Further assuming that the waves propagate as in free space, such diffraction would occur given two waves with propagation vectors drawn from points $O$ and $H$ on the reciprocal lattice and intersecting at the point $L_a$, see Figure 7. $L_a$ is known (after Ewald) as the Laue point and is the intersection of two spheres centered at $O$ and $H$, each having radius $k$.

Actual waves propagating **in** a real crystal interact with the medium resulting in an index of refraction $n$ where

$$n = \left(1 + \chi_o / 2\right).$$

In Figure 7, the Lorentz point $L_o$ is the intersection of the other set of spheres centered on the same two reciprocal lattice points $O$ and $H$ and having radii $nk$. Since, for X-rays, the index of refraction is smaller than 1 this set of concentric spheres is located inside the first set. It would seem that for diffraction in an actual crystal to occur, the resulting wavevectors $\mathbf{K_o} = \mathbf{OP}$ ,for the refracted wave, and $\mathbf{K_h} = \mathbf{HP}$ , for the reflected wave, would have to extend from the points $O$ and $H$ and intersect at the Lorentz point $L_o$. In fact, as will be seen, under diffraction conditions for perfect crystals, the wavevectors intersect at certain points $P$ lying between the two sets of spheres (Figure 7). This new sort of diffraction, which is only approximated by ordinary Bragg diffraction (though the accuracy increases near the edges of the reflection domain), is called *dynamical* diffraction.

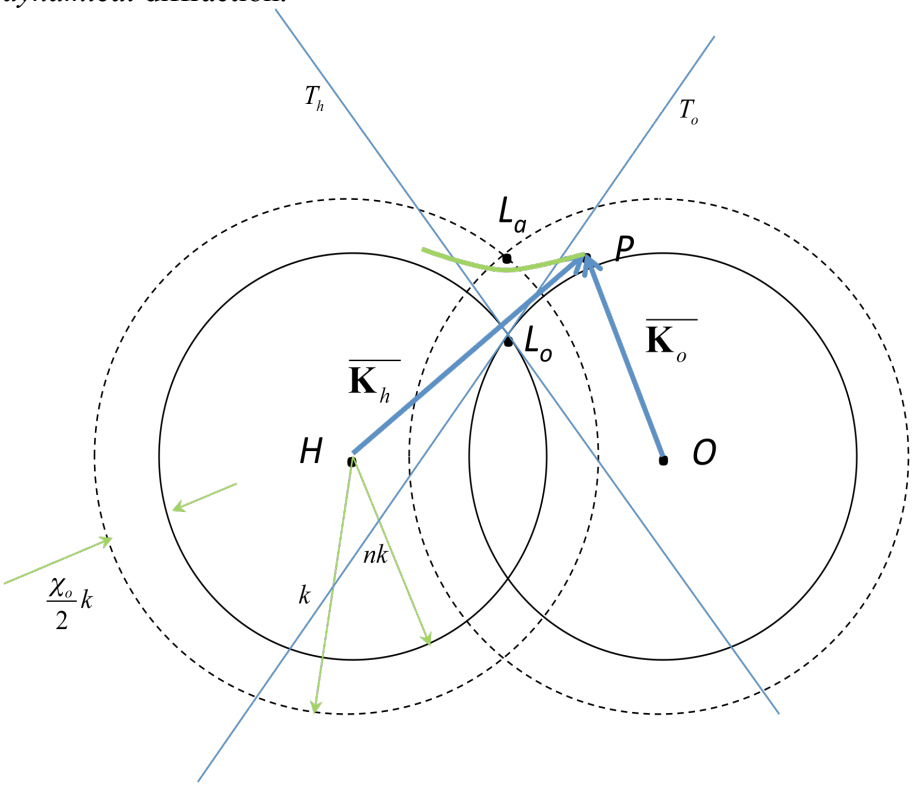


Figure 7: Illustration of the mathematical framework for the determination of Bragg diffraction in the dynamical theory (green line represents dispersion surface in figures 5 and 6).

## *Dispersion equations*

In the development of the equations for dynamical diffraction of perfect crystals we begin with Maxwell's equations. A periodic complex dielectric constant is used to describe the medium of the crystal. It is also assumed that wave solutions conform to Bragg's law, in the form $\mathbf{K_h} = \mathbf{K_o} + \mathbf{h}$ . We then arrive at a system of two equations in the field amplitudes $\Psi_o$ and $\Psi_h$:

$$X_o\Psi_o - \frac{k\chi_{\bar{h}}}{2}\Psi_h = 0$$

$$-\frac{k\chi_h}{2}\Psi_o + X_h\Psi_h = 0.$$

Where $k = 2\pi/\lambda$ is the wavenumber of free space, incident radiation. Solving this system yields the dispersion equation

$$X_o X_h = \frac{k^2 \chi_{\bar{h}} \chi_h}{4}$$

In particular, the value of $X_o$ represents the difference between the wavevector inside the crystal and the vacuum value correct for the average refractive index and similarly for $X_h$. Referral must be made to Figure 8 again in order to better understand the paramaters $X_o$ and $X_h$.

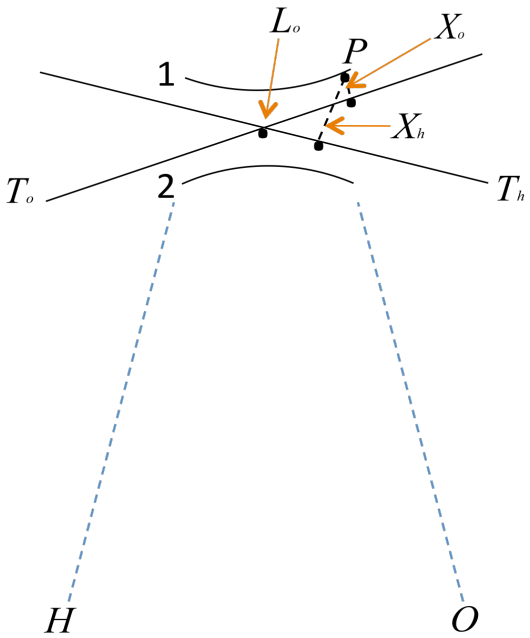


Figure 8: Method for computing diffracted beam paths using the dispersion surface

To get an idea of the proper scale of this figure, if the distance between $L_o$ and $L_a$ were as shown in the figure, the length of the propagation vectors would be on the order of the length of a football field. Given this scale, for points $P$ near the Lorentz point $L_o$, the spheres passing through it can be represented by their tangents, the lines $T_o$ and $T_h$ (Figure 8), which intersect at $L_o$. Hence, for a given point $P$, $X_o$ and $X_h$ can be seen (Figure 8) to represent the difference between the wavenumbers $OP$ and $HP$ of the refracted and reflected wave, respectively, and $nk$. Ewald refers to this distance as the resonance error. It can be shown that it can never equal zero because the waves in the resulting wavefield would have infinite amplitudes. In the above system of equations, this condition would result in the equations not having a unique solution. The $\chi_h$ terms are the dielectric susceptibility in the direction of incident excitation and correspond to a measure of polarization. Hence it is synonymous with and therefore often called the polarizability in many texts. While this can be complex, for a silicon 220 direction it is a real scalar of value $\chi_h$ = -9.396 x $10^{-6}$. This value incorporates the Fourier component of the structure factor in this direction that, in turn, is computed from the charge distribution $\rho(\mathbf{r})$ in a unit cell. These values can be computed from

$$F_h = \int_{\text{All reciprocal lattice points}} \rho(\mathbf{r}) \exp\left(-2\pi i (\mathbf{h}.\mathbf{r})\right) d\tau = F_{rh} + iF_{ih}$$

$$\chi_h = \frac{R\lambda^2}{\pi V} F_h$$

$$\chi_{rh} = \frac{R\lambda^2}{\pi V} F_{rh}$$

$$\chi_{ih} = -\frac{R\lambda^2}{\pi V} F_{ih}$$

Where $R = 2.8179402894(58)$ x $10^{-15}$ m is the classical electron radius constant, $\lambda$ is the wavelength of incident radiation (=0.1544390 nm, 8.02783 keV) and $V$ is the volume of the unit cell (0.16019 ($nm^3$)) and $F_h$ is the structure factor. Because of the symmetry of this cubic crystal the structure factor is simply given by

$$F_h = -8 f_1$$

Where $f_1$ is the scattering factor which, for silicon can be obtained from Figure 10 and Figure 8.

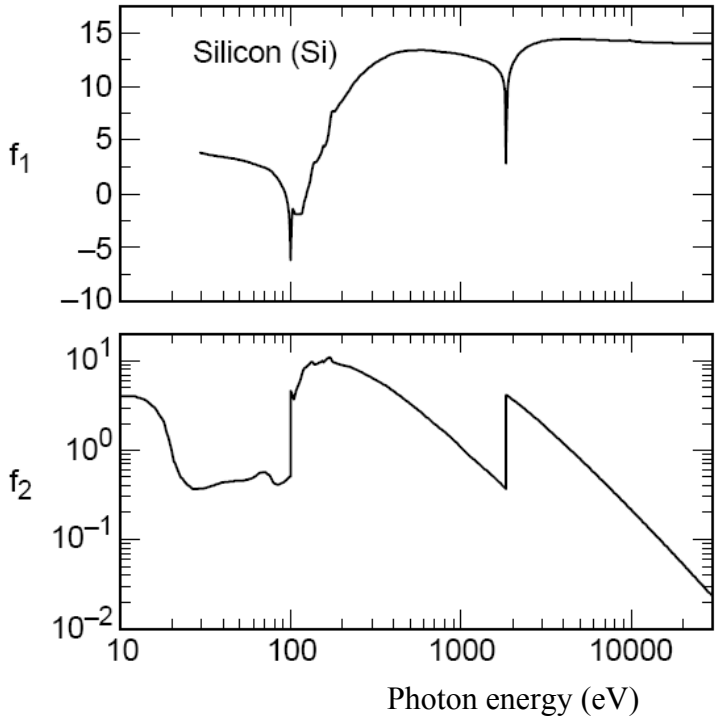


Figure 9: Scattering f 93)

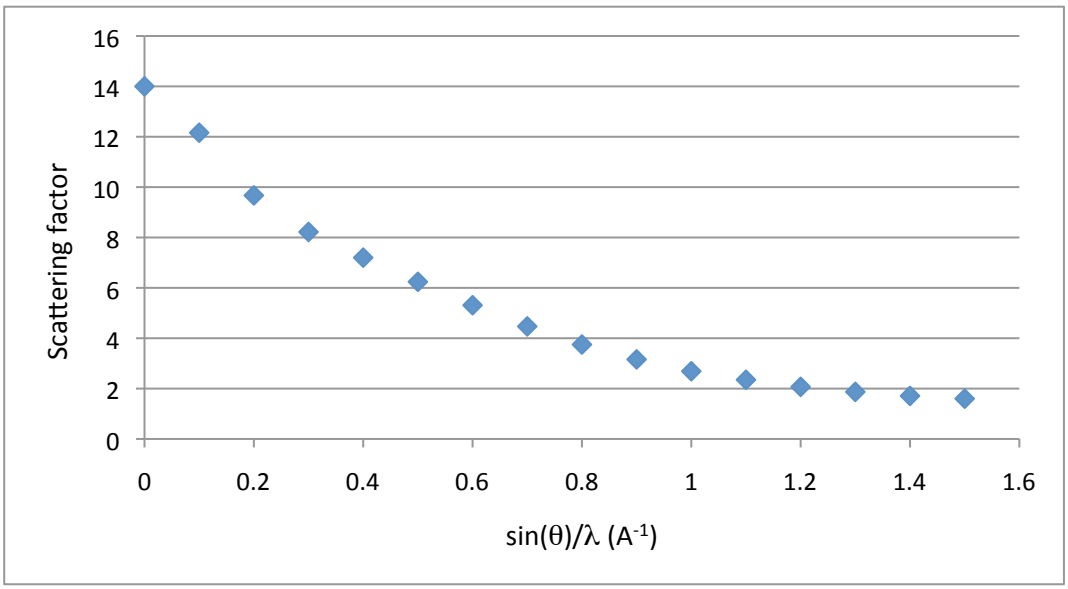


Figure 10: Real part of scattering factor as a function of Bragg angle (data taken from International tables for x-ray crystallography vol. III).

For the 220 reflection the Bragg angle of 0.413866 yields a scattering factor of 8.7943 by extrapolation in Figure 10 from which a final value for the dielectric susceptibility $\chi_h$ is 9.3961 x $10^{-6}$ a value a little less than 2% higher than that quoted in Authier.

## *Determination of the tie points on the dispersion surface*

Next we consider the determination of the tie points from the incident boundary conditions. Two sets of boundary conditions must be applied: those regarding the incident beam external to the crystal and the refracted wavevectors inside the crystal ( $\mathbf{K}_{\mathbf{o}}^{i}$ and $\mathbf{K}_{\mathbf{o}1}{}^{1}$, where $d$ refers to an incident beam for Laue refraction and the 1 in the subscript indicates that we are considering branch 1 of the dispersion surface, see Figure 12).

[1] See Table 2 regarding the meanings of the superscripts and subscripts of the various propagation vectors $(K)$

The first set of boundary conditions are in accord with the *Snell-Descartes* law: the tangential components of the incident and refracted wavevectors must be continuous across the interface boundary. Stated differently, the difference between the incident and refracted wavevectors must lie along the surface normal, $\mathbf{n}$, in our case this will always be perpendicular to the plane of refraction. The tie point $P$ is therefore determined by the intersection of a line with direction $\mathbf{n}$ passing through $M$, with branch 1 of the dispersion curve (Figure 12). In practice the distance between the two sets of tangents is proportionate to the unit decrement. Consequently, it is reasonable for all practical purposes to consider the tangents to be parallel. Additionally, we are only considering branch 1; branch 2 is strongly absorbing and can be ignored.
The point $M$, however, is determined by the deviation, $\Delta\theta$, from the ideal kinematic Bragg reflection angle. We see in Figure 12 that this small deviation is equal to $\overline{L_a M}/k$. From Figure 12it can be shown that

$$\frac{X_{o1}}{\gamma_o} - \frac{X_{h1}}{\gamma_h} = \overline{M_o M_h},$$ and

$$\overline{M_o M_h} = \overline{L_o M_o}\frac{\sin 2\theta_B}{\gamma_h}.$$

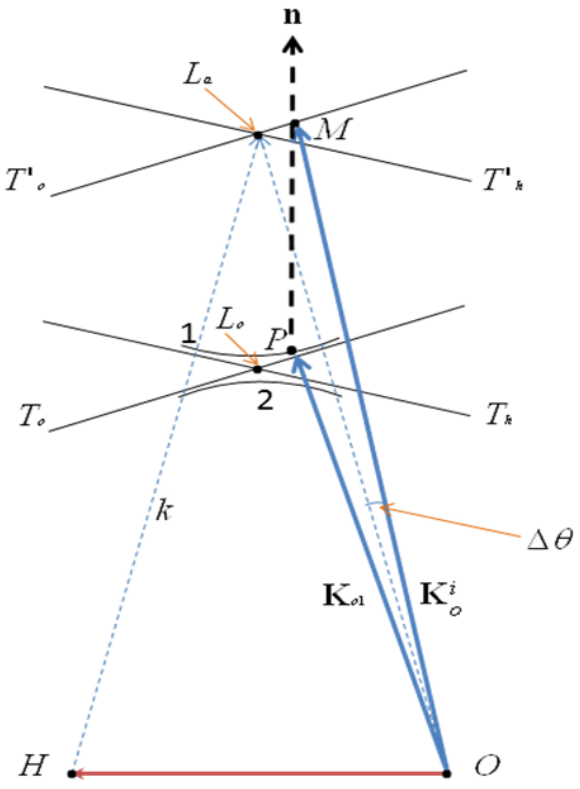


Figure 11: Boundary conditions for determination of the tie point

$\psi_o$ is the angle between the surface normal $\mathbf{n}$ and the incident propagation vector $\mathbf{s}_o$ and Here $\gamma_o = \cos\psi_o$ and $\gamma_h = \cos\psi_h$ are both equal to $\cos\theta_B$ since we are concerned only with the (220) planes of silicon and these are perpendicular to the crystal surface. Since

$$\overline{L_o M_o} = \overline{L_a M},$$

it follows that

$$\overline{M_o M_h} = k\Delta\theta\frac{\sin 2\theta_B}{\gamma_h}.$$

We have

$$\frac{X_{o1}}{\gamma_o} - \frac{X_{h1}}{\gamma_h} = k\Delta\theta\frac{\sin 2\theta_B}{\gamma_h}$$
$$X_{o1} - X_{h1} = k\Delta\theta\sin 2\theta_B$$

(*).

And so it is seen that the distances of the tie point from $T_o$ and $T_h$ and thus the tie point $P$ itself is indeed determined in terms of the deviation from the exact Bragg angle.
The dispersion equation can be written

$$X_{o1}X_{h1} = k^2\chi_h\chi_{\bar{h}}/4 = \frac{1}{4\Lambda_o^2}$$

where

$$\Lambda_o^{-1} = k\sqrt{\chi_h\chi_{\bar{h}}} = k\chi_h$$

is called the Pendellosung distance. Now, set

$$\eta = \Delta\theta/\delta_{os}$$

where

$$\delta_{os} = \frac{\lambda}{\Lambda_o \sin 2\theta_B} = \frac{\lambda}{\sin 2\theta_B}$$

is half the Darwin width. Then we can rewrite the equation governing position of the tie points as

$$X_{o1} - X_{h1} = \frac{\eta k\chi_h}{\sin(2\theta_B)}\cos(\theta_B)$$

We have the following expressions for the tie point in terms of the deviation parameter:

$$X_{o1} = \frac{\cos(\theta_B)}{2\Lambda_o}\left[\eta + \sqrt{\eta^2+1}\right]$$

$$X_{h1} = \frac{\cos(\theta_B)}{2\Lambda_o}\left[\eta + \sqrt{\eta^2+1}\right]$$

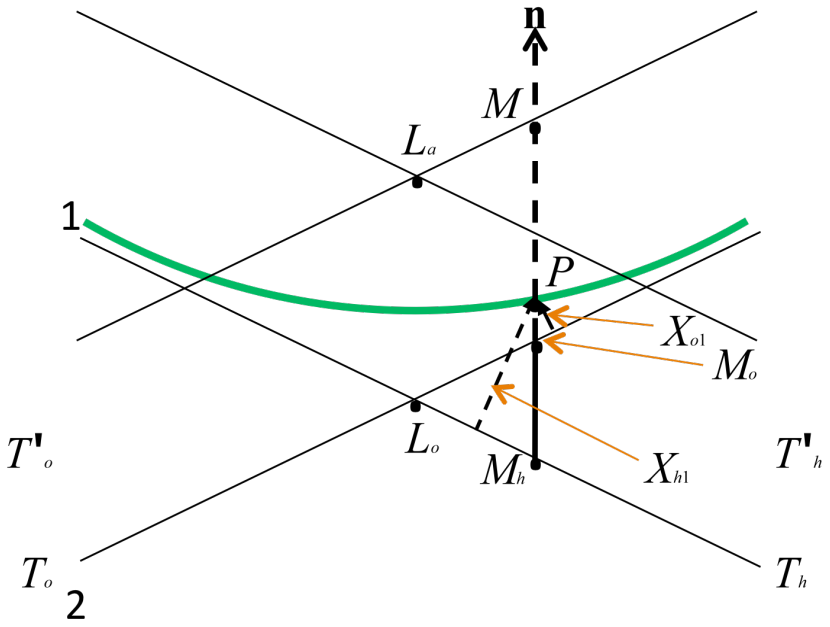


Figure 12: Geometric model for determination of the tie points on the dispersion surface.

Table 2: Parameters of relevance for dynamical diffraction studies for 220 silicon reflection using $Cuk\alpha$ radiation

| Parameter | Description |
|---|---|
| $\chi_o, \chi_h$ | Fourier component of the dielectric susceptibility: for the (220) reflection of $CuKa$ on silicon, $\chi_o = -1.5142\times10^{-5}$ and $\chi_h = -9.24\times10^{-6}$ |
| $k = 1/\lambda$ | Wavenumber in vacuum |
| $\mathbf{K}_{oj}, \mathbf{K}_{hj}$ | Wavevectors of a wavefield inside the crystal with $j$ denoting dispersion surface branch line. |
| $\mathbf{K}_o^i$ | Wavevector of the incident wave external to the crystal |
| $\Lambda_o$ | Pendellosung distance |
| $X_o, X_h$ | Distances of the tiepoint from the spheres passing through the Lorentz point. |
| $\Psi_o, \Psi_h$ | Electric field amplitudes from solutions to Maxwell's equations in the crystal |
| $\delta_j (j = 1,2)$ | |
| $\lambda$ | Wavelength |
| $\Lambda_o$ | Pendellosung distance |
| $\gamma_o, \gamma_h$ | Cosine of the angle between the normal to the crystal surface and the incident and reflected direction, respectively |
| $\theta_B$ | Bragg angle |
| $\Delta\theta$ | Departure from Bragg's angle of the incident beam |

References

Batterman, B. W. and H. Cole, *Rev. Mod. Phys.*, **36**, 681-717 (1964)

Bonse U. and Hart M., 1965, Principles and design of Laue-case x-ray interferometers, Zeitschrift fur Physik, **188**, 154 – 164.
Ewald P.P., *Acta Cryst.*, **11**, 888-891.
B. L. Henke, E. M. Gullikson, and J. C. Davis, "X-Ray Interactions: Photoabsorption, Scattering, Transmission, and Reflection at $E$ = 50–30,000 eV, $Z$ = 1–92," *At. Data Nucl. Data Tables* **54,** 181 (1993).

4 Quantitative imaging from scattered fields, Terahertz imaging and spectroscopy (Dr. Fiddy)

**Negative index metamaterials and superresolution imaging**

Our motivation was to understand how to assemble a practical metamaterial with a refractive index close to -1 which can be used for high resolution (sub-wavelength scale) imaging. We did not expect to be able to make the "perfect" lens with these properties but, by adjusting the components of our metamaterial, to maximize the transfer of evanescent waves from the 3D scattering object to the image domain. Transfer of evanescent waves, or equivalently, high spatial frequencies with $k > k_0$, will lead to a field pattern in the image domains exhibiting superoscillations. It will remain an important and as yet unanswered question how to relate this field pattern to the intrinsic material properties of the object to be imaged: this represents an inverse scattering problem to be addressed in a later publication. The successful transfer of some bandwidth of evanescent waves will improve resolution and thereby increase the effective number of degrees of freedom of the imaging system. Some evanescent waves might be coupled into propagating waves which of course is the express purpose of a hyperlens. The latter is highly desirable but the inverse scattering problem remains and there is the potential for the cross-contamination of converted evanescent waves into k-vectors associated with propagating scattered field components from the object. We view the transfer of evanescent waves as inherently a multiple scattering and element-to-element coupling phenomenon, physically, Consequently, the elements or meta-atoms used in the design of our bulk imaging metamaterial. If the ideal metamaterial for perfect imaging has an index of -1, then it is likely that the optimized but practical metamaterial we seek will also exhibit a negative index. This property is well known to be associated with group and phase velocities having opposite directions. Normally, we attribute a positive index to naturally occurring materials based on its approximate description in terms of a large number of dipole radiators, each representing an atom in that material. The sum of the fields from a sheet of diploes can be calculated and it is found to lead to an overall phase retardation with respect to the incident or driving field, and this delay is considered synonymous with a positive refractive index. By analogy with this one might expect that a combination of meta-atom location and non-dipole-like radiation patterns could provide an overall phase advance, characteristic of a negative refractive index. The 3D scattering or radiation (beam) pattern from each meta-atom determines the phase, amplitude and direction of the wave transferred to its neighbors in the metamaterial [1]. Provided these meta-atoms are in close proximity to each other, there is the opportunity for evanescent waves to be coupled and transferred through the structure. One usually assumes phase advance or retardation shifts accumulate gradually during the wave's propagation through a material, to shape emerging

wavefronts and beams. Meta-atoms, however, can introduce abrupt phase changes over scales shorter than the wavelength. Even a two-dimensional array of resonant meta-atoms with spatially varying phase response and subwavelength separations can impose extreme phase shifts (even discontinuities) on propagating electromagnetic waves, leading to anomalous reflection and (negative) refraction phenomena, which have been observed. Our question is how do we exploit this to faithfully transfer the widest bandwidth of evanescent waves in a practical metamaterial.

**Methods to identify negative refraction and/or negative refractive index**

There are several methods to identify negative refractive properties in a metamaterial. Simple examples include i) negative refraction phenomenon observed in a prism made of a negative refractive metamaterial [2]; ii) observation of a backward wave and phase advance in a negative refractive index metamaterial [3, 4]; iii) the transmission spectrum of evanescent incident waves shows pass bands (i.e. if there is no negative refraction, a structure illuminated with evanescent waves will show no transferred wave) [5]. Alternatively, one may also calculate the refractive index of a metamaterial using, for example, the S-parameter retrieval method [6, 7], to determine if the metamaterial shows negative refractive index.

The S-parameter retrieval method is widely used to obtain effective parameters of a metamaterial, including refractive index (n), permittivity (ε), and permeability (μ).We note that this approach has been scrutinized in some detail when applied to metamaterials, specifically because of the inherent periodicity of most metamaterials (see [7]) and great care must be taken in interpreting the calculated estimates for refractive index. In the retrieval method, S-parameters ($S_{11}$ and $S_{21}$ for example) are obtained experimentally and/or numerically. The impedance (Z) and n are then obtained by the following equations [6].

$$Z = \pm\sqrt{\frac{(1+S_{11})^2 - S_{21}^2}{(1-S_{11})^2 - S_{21}^2}} \quad (1)$$

$$e^{ink_0d} = \frac{S_{21}}{1 - S_{11}\dfrac{Z-1}{Z+1}} \quad (2a)$$

$$n = \frac{1}{k_0 d}\left\{\left[\left[\ln\left(e^{ink_0d}\right)\right]'' + 2\pi m\right] - i\left[\ln\left(e^{ink_0d}\right)'\right]\right\} \quad (2b)$$

where (‘) and (“) denote the real part and imaginary part operators respectively, d is the thickness of the material in the propagation direction, and m is an integer that defines the branch of the complex logarithmic function. For a passive medium, the conditions that Z’ ≥ 0 and n” ≥ 0 (or equivalently, $|e^{ink_0d}| \leq 1$ [6]) must be fulfilled. The branch index m is zero at low frequencies, and the value of m for higher frequencies is determined by the mathematical continuity of the parameters, as described in [6].

**Double layered S-shaped structures**

It has been reported that S-shaped resonators (also called meander line structure [8-10]) can support negative refractive index properties and thus be used to compose a metamaterial superlens [11, 12]. In this study, two different double-layered “S”-like structures are investigated

(Fig.1). The structures under study compose of S-shape resonators (copper) printed on the opposite sides of a dielectric substrate (FR4, ε=3.9). One contains two identical S-shape resonators (the parallel case) and the other one consists of mirrored S-shape resonators (the mirrored case). The mirrored case is very similar to the S-shaped split ring resonator (SRR) proposed by Chen et al. [11]. Here the dielectric constant of the materials used is assumed constant as a function of frequency for simplicity. Both structures are assumed continuously connected in the y-direction and the dimensions of the structures are chosen so that the resonant frequencies are in the range of 7 GHz to 12 GHz (Fig.1(c)). The ratio of vacuum wavelength to unit cell size in the propagation direction is between 3.9 (at 7GHz) and 6.56 (at 12 GHz). As a result of the structure's strong dispersion near resonant frequencies, it is not simple to specify how well such a meta-atom assembled into a metamaterial will behave as an anisotropic but continuous effective medium over the frequencies in this range. However, our primary goal is to investigate the transfer of evanescent waves since successful transfer, even if associated with distortions, need not preclude the successful computation of a superresolved image from the measured fields. A commercial software package, COMSOL (v.4.2), based on finite element method, is used to obtain S-parameters.

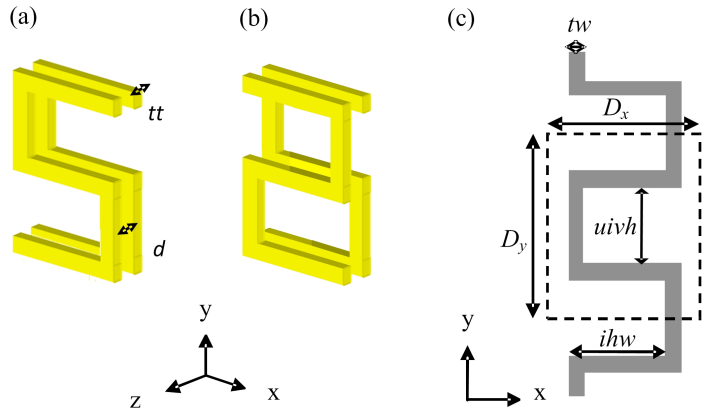


Figure 1. Basic double-layered S structures under study. Meta-element of (a) the parallel case (b) the mirrored case, (c) dimensions of the structures with dimensions indicated, where uivh=3.2 mm, ihw=3.84 mm, tw=0.64 mm, tt=38 μm, and d=1.6 mm. This structure is made of copper and is printed on the opposite sides of a dielectric substrate (FR4, ε=3.9) with the unit cell size $D_y$=7.68 mm and $D_x$=6.4 mm (indicated by the dashed rectangle in (c)). Both structures are assumed continuously connected in the y-direction.

**The parallel case**

We started our investigation with the parallel design (Fig.1(a)), assuming plane waves are normally incident on the y-z plane and propagating along the +x-direction with E-field polarized in y-direction. Periodic boundary conditions are applied on the domain boundaries parallel to the x-y plane and x-z plane so that the structure is assumed to be repeated infinitely in y-direction and z-direction respectively. The retrieved effective refractive index of one row, two rows, and three rows of the parallel S in the x-direction are displayed in Fig. 2, as a function of frequency. As seen in the figure, the retrieved refractive index of different rows of the parallel S are very similar, suggesting that a thin row of such parallel S can represent an effectively homogeneous

metamaterial slab without considering the coupling between the neighboring rows. The loss is close to zero in the range of 9.1 GHz to 9.7 GHz, where the corresponding n' gradually changes from 0 to 1.8. This is an intrigueing and important observation suggesting that for a chosen fixed frequency, the geometry of this parallel S structure could be altered in order to define any index over this range while maintaining low loss,. However, for the given geometrical placement and material properties used, we have not found a condition for this parallel design to support a negative refractive index.

It was reported that negative refractive index can be achieved by breaking the geometrical symmetry (e.g. symmetry between the two stacked layers) and/or structural symmetry (i.e. the symmetry of the meta-atom structure) [13, 14]. We have also broken the structural symmetry of the S metamaterial by considering two rows in the propagation direction with one row shifted by $0.5*D_y$ and 3*tw, the retrieved results are very similar to the ones obtained in Fig. 2 and do not support a negative refractive index.

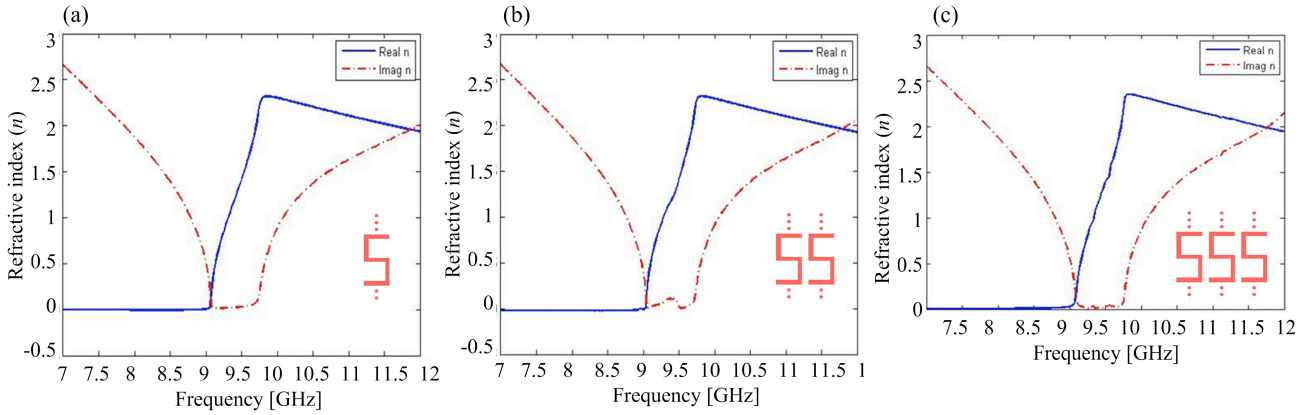


Figure 2. Effective refractive index of different rows of the parallel S structures in the x-direction. (a) One row, (b) two rows, and (c) three rows.

**The mirrored case**

Similarly, we obtained the effective refractive index of the mirrored structure (with the same dimensions as the parallel case, indicated in Fig. 1(c)) as shown in Fig. 3(a). This structure was first studied in detail in [4]. The retrieved refractive indexes of one to three rows of the mirrored S in the propagation direction also match well, indicating that the properties of a single sheet dominate the resulting bulk metamaterial's properties.. This structure supports a low loss negative refractive index from 7.8 GHz to 11 GHz, and n is approximately equal to -1 around 9.09 GHz. The low-loss frequency range in this case is wider compared to that for the parallel case.

To break structural symmetry of this S metamaterial, we considered the two rows in x case, with one row shifted by $0.5*D_y$ and 2*tw (Fig.3(b) and (c)), the retrieved results are very similar to those obtained without breaking structural symmetry. This result is encouraging, suggesting some fabrication tolerance would be allowed for such a metamaterial, important if assembling it from layers and for eventual optical applications. Compared to the parallel cases, where a step-like curve is introduced in the retrieved refractive index spectrum when one row is shifted by

0.5*$D_y$, the mirrored case does not have this trend.
Coupling between neighboring layers was also investigated. Fig. 4 shows the retrieved refractive index for different periodic spacings in the z-direction, assuming there is only one row in the forward (x) propagation direction. When the period in the z-direction increases (i.e. coupling becomes weaker), the low-loss frequency range of negative refractive index becomes smaller, and the frequency where n = -1 occurs also increases with $D_z$. The complex nature of the scattering pattern from a single meta-atom shows considerably asymmetry of the field in x and z but symmetry with the symmetry of the structure in y.

Fig. 5 shows how the refractive index of the mirrored case also changes with different trace width, another degree of freedom at our disposal for controlling the scattering and coupling between meta-atoms. When the trace width of the mirrored case is reduced from 640 μm to 80 μm, in general the frequency range of low-loss negative refractive index becomes smaller. The frequency at which n = -1 occurs, increases with reducing trace width, consistent with a reduction in both the capacitance and the inductance of the meta-atom. The curve shown in the tw=160 μm case is an example demonstrating the effects due to structure periodicity [15]. We normally expect a resonance-related negative index to be on the high frequency side of the resonant frequency. The figure for tw = 80 microns which has the highest resonant frequency, looks like a classical resonance phenomenon over our frequency range. For the larger trace widths shown, the index behavior is indeed at a higher frequency than the resonant frequencies which are not shown (< 7GHz). When tw=80 μm, there is no negative refractive index present but a sharp change of refractive index from 0 to 2.2 then back to 0 from 8.8 GHz to 9.3 GHz.

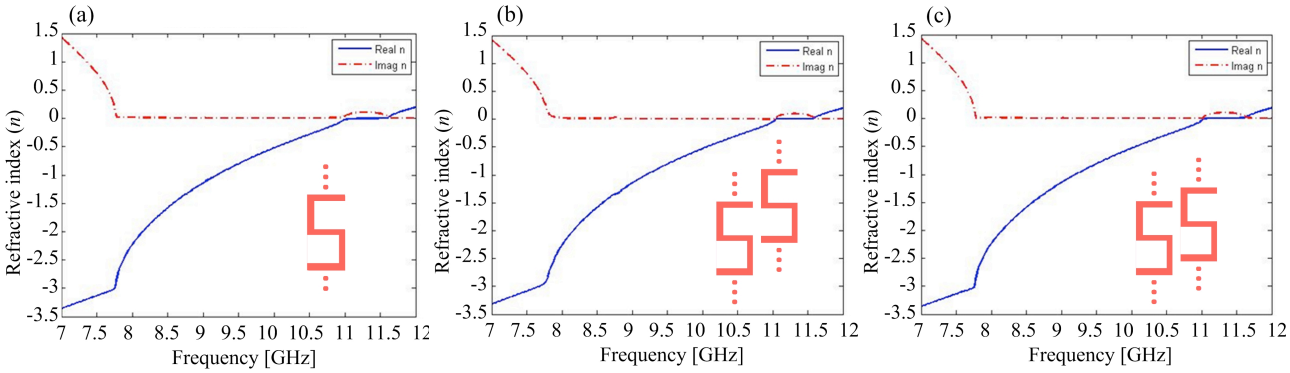


Figure 3. Effective refractive index of different rows of the mirrored S structures in the x-direction. (a) One row, (b) two rows, and (c) three rows. (d) Two rows with one row shifted by $D_y/2$=3.84 mm (e) two with one row shifted by 2*tw=1.28 mm

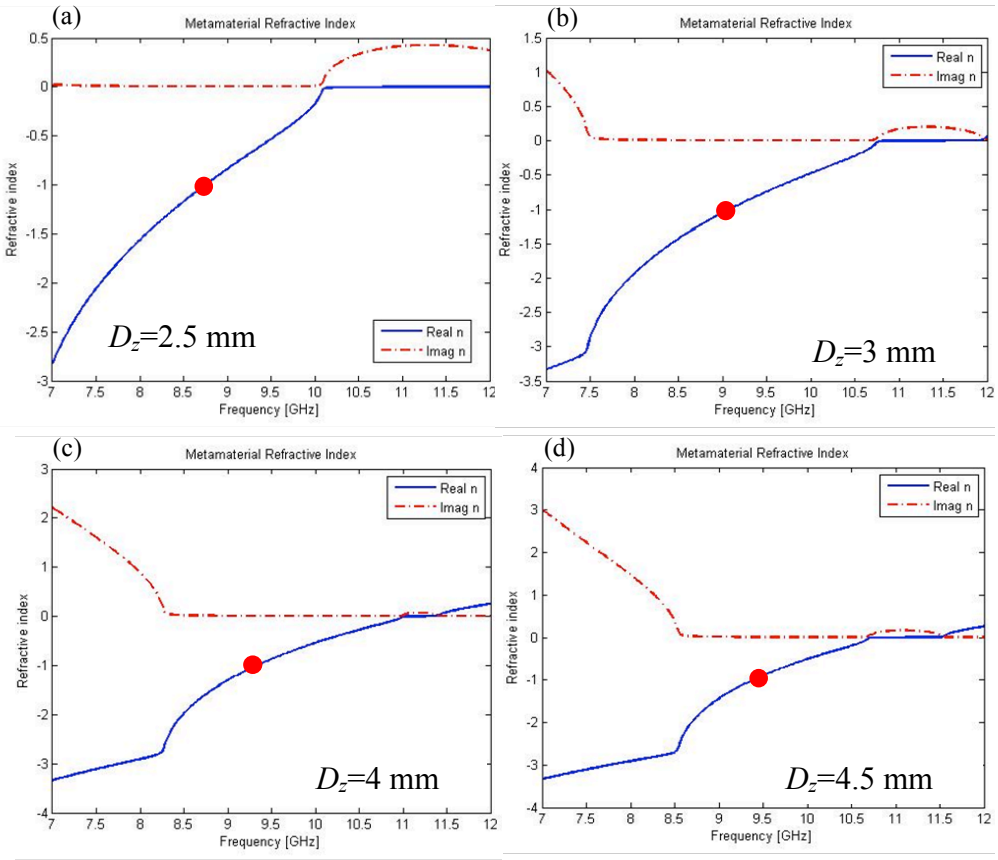


Figure 4. Effective refractive index of the mirrored S structures with different values of the period in the z-direction ($D_z$). Red dot indicates where n=-1 occurs

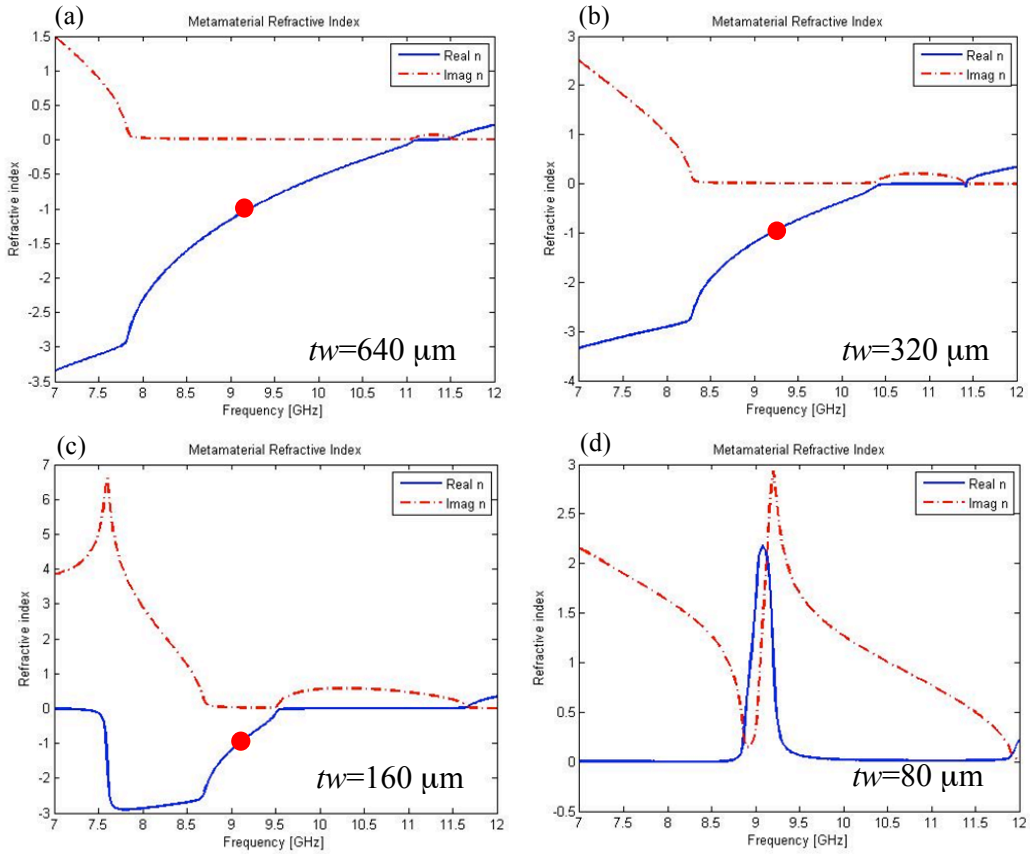


Figure 5. Effective refractive index of the mirrored S structures with different values of the trace width (tw), where uivh=3.2 mm and ihw=3.84 mm are assumed constant. Other design parameters also remain the same. Red dot indicates where n=-1 occurs.

**Conclusions**

We have described as systematic study into the design of a bulk metamaterial to be used for superresolved imaging. The meta-atoms employed are of a well-known type, parallel or mirrored S structures, which others have demonstrated are capable of supporting a negative index. Our point in this paper is that in developing practical metamaterials comprised of such meta-atoms there are several degrees of freedom available to enable the improved transfer of evanescent waves from the object to image domains. Having set a desired wavelength range of operation and a size for the meta-atoms, we presented results showing how adjustments to the proximity of meta-atoms to each other and the metal trace width, can control the effective complex refractive index of a periodic bulk metamaterial. We focused on a frequency range over which losses could be controlled to be relatively low (of the order of + i 0.02) and the real part of the refractive index could be varied from $-3 < n < 2.5$. For high resolution imaging applications, we have most interest over the design parameter set for which $n \sim -1$ and losses are low. We established that bulk metamaterial properties are largely dictated by a periodic sheet of meta-atoms just one layer thick in the propagation direction. In other words, at least for the cases studied, the bulk metamaterial properties were not strongly influenced by the number of additional layers in the x direction, nor did the alignment of these layers with respect to y and z

greatly affect the overall complex refractive index for this frequency range. The choice of trace width did modify the low loss and negative index regime for the mirrored structure and that modification was explained in terms of the associated dependence of the resonant frequency on trace width. Numerical simulations confirm a backward wave with low loss at the predicted frequencies but finite size effects and determining the functional dependence of the evanescent wave transfer function on the parameters we adjusted is an on-going exercise and will be the basis of future work.

**REFERENCES**


[1] Yu, N., Genevet, P., Kats, M. A. et al., "Light Propagation with Phase Discontinuities: Generalized Laws of Reflection and Refraction," Science, 334(6054), 333-337 (2011).

[2] Shelby, R. A., Smith, D. R., and Schultz, S., "Experimental Verification of a Negative Index of Refraction," Science, 292(5514), 77-79 (2001).

[3] Moss, C. D., Grzegorczyk, T. M., Zhang, Y. et al., "Numerical Studies of Left Handed Metamaterials," Progress In Electromagnetics Research, PIER, 35, (2002).

[4] Chen, H., "Negative refraction of a combined double S-shaped metamaterial," Appl. Phys. Lett., 86(15), 151909 (2005).

[5] Smith, D. R., Padilla, W. J., Vier, D. C. et al., "Composite Medium with Simultaneously Negative Permeability and Permittivity," Physical Review Letters, 84(18), 4184-4187 (2000).

[6] Chen, X., Grzegorczyk, T. M., Wu, B.-I. et al., "Robust method to retrieve the constitutive effective parameters of metamaterials," Physical Review E, 70(1), 016608 (2004).

[7] Smith, D. R., Vier, D. C., Koschny, T. et al., "Electromagnetic parameter retrieval from inhomogeneous metamaterials," Physical Review E, 71(3), 036617 (2005).

[8] Fu, L., Schweizer, H., Graebeldinger, H. et al., "Metallic Meanders: an Optimal Design for Visible Negative Index Metamaterials." 362~364.

[9] Güney, D. Ö., Koschny, T., Kafesaki, M. et al., "Connected bulk negative index photonic metamaterials," Opt. Lett., 34(4), 506-508 (2009).

[10] Tang, W. X., Zhao, H., Chin, J. Y. et al., "Negative index material composed of meander lines and SRRs," Progress in Electromagnetics Research B, 8, 103~114 (2008).

[11] Chen, H., Ran, L., Huangfu, J. et al., "Left-handed materials composed of only S-shaped resonators," Physical Review E, 70(5), 057605 (2004).

[12] Khan, M. F., and Mughal, M. J., "Modified Single Side Paired S-ring Resonators."

[13] Abdeddaim, R., Ourir, A., and De Rosny, J., "Realizing a negative index metamaterial by controlling hybridization of trapped modes," Physical Review B, 83(3), 033101 (2011).

[14] Kanté, B., De Lustrac, A., and Lourtioz, J.-M., "Low loss negative index metamaterials with one type of meta-atom," Photonics and Nanostructures - Fundamentals and Applications, 8(2), 112-119 (2010).

[15] Koschny, T., Markoš, P., Economou, E. N. et al., "Impact of inherent periodic structure on effective medium description of left-handed and related metamaterials," Physical Review B, 71(24), 245105 (2005).


5 Multiphoton and Raman microscopy (Dr. Her)

## Introduction

Our goal in this sub-project is to develop nonlinear optical imaging facility at UNCC that will have the capability to perform three-dimensional imaging of cells and tissues with high-resolution and optical contrast. This microscope is configured to have wide laser tuning range, and integrate the laser system, photomultiplier detectors, spectrometers, and high-sensitivity imaging system to be used for a wide variety of imaging needs. Our accomplishments to date in each of these categories are summarized below.

## Hardware Instrumentation

Hardware instrumentation is consisted of four major sections: light source, optics, scanning stage, and light detection.

### Laser

The pump laser was upgraded on Feb 2010 from 8 W to 10 W. This enables the tuning range of our existing femtosecond laser from 750 – 900 nm to 700-1000 nm. This upgrade enables fluorescent detection of a wide range of fluorescent markers. The femtosecond laser and its wavelength tuning curve are shown in **Error! Reference source not found.**.

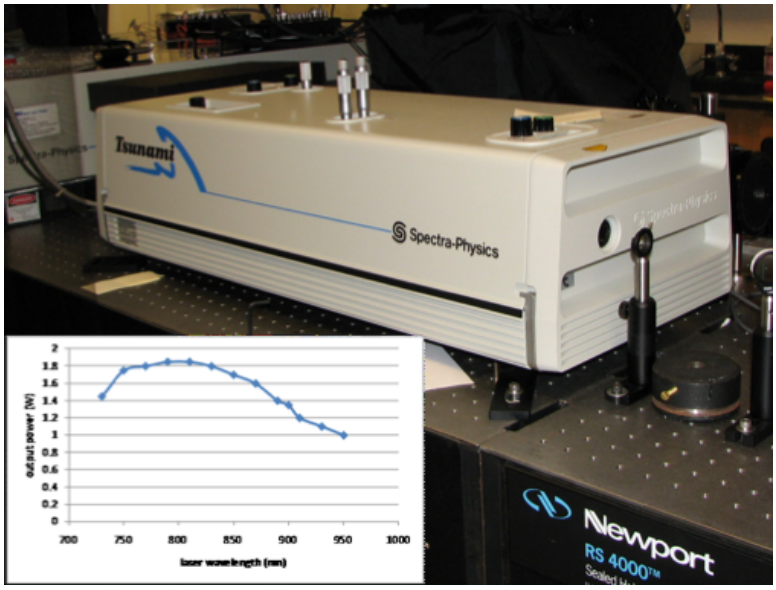


Figure 13: Femtosecond pulsed laser for two-photon fluorescence excitation. Inset shows the wavelength tuning curve.

### Optics

The optics associated with this microscope are constructed by us from either commercial off-shelve optical elements and optomechanics, or customized machined by us. In contrast to most home-built microscopes where all optics is layout in a 2D plane made of an optical breadboard, here we employ a unique 2+1 D architecture in which the optics for excitation is laid in the bottom floor, while the fluorescence detection optics in the top floor of the optical breadboard. This design has the advantages of 1) separate excitation and detection beam paths to minimize

cross talk to ensure larger single-to-noise ratio and higher sensitivity, 2) smaller footprint and better mechanical stability.

Besides the unique 2+1 D architecture, the optics falls into the following sub-assemblies:

1) Optical telescope to expand the laser beam size 4 times to overfill the back aperture of the microscope objective to achieve maximum resolution,
2) Excitation optics (bottom floor) including dichroic beam splitter mount, cube housing, and its stand.
3) Fluorescence detection arm optics including folding mirror, lens, pinhole, and a photomultiplier tube.
4) A unique focus-monitoring scheme based on confocal mechanism by picking up the back reflection from the microscope objective and focusing it to a CCD camera to monitor the laser focus under the microscope objective. This significantly eases the focus drift issue and enhances image quality and reproducibility.

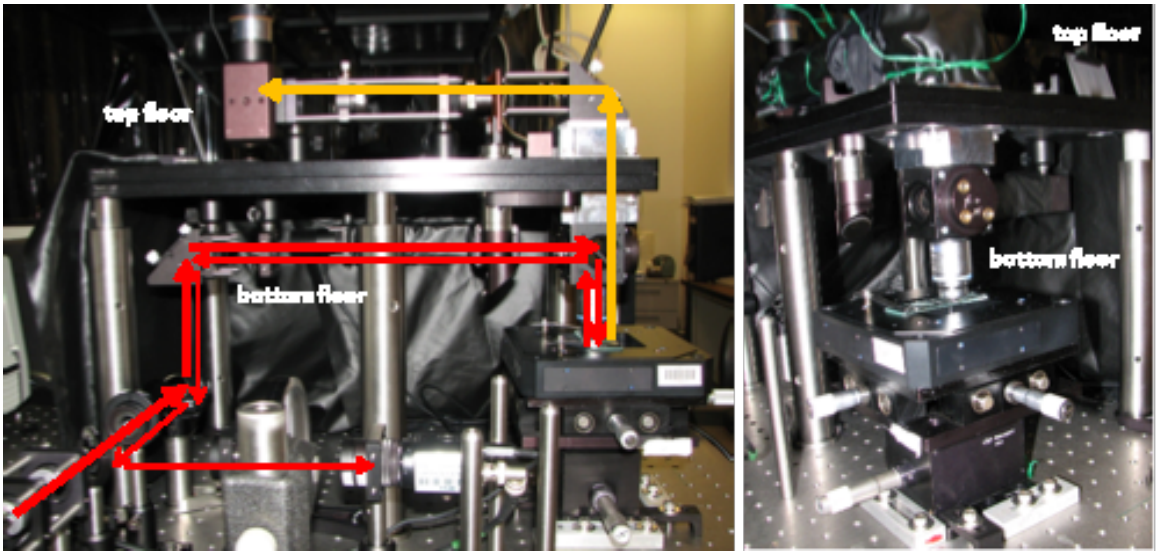


Figure 14: Photos of the microscope and optical beam paths. Thick red: excitation beam. Thin red: reflected excitation beam for confocal monitoring of laser focus in the microscope objective. Thick yellow: fluorescence detection beam path.

**Scanning stage**

In the design we raster scan the sample with respect to the laser focus. Substrate scanning is accomplished by a close-loop piezo scanner with 300 μm scanning range in all three axes. Additional coarse translation of the substrate is made by a manual XY and a manual Z stages. The close-loop piezo scanner provides a spatial accuracy of 1 nm and a resolution of sub-nanometer in all three axes.

## Data acquisition and Software development

We have developed our own LabView code to perform image acquisition and signal processing. The code is comprised of four segments which are detailed below. Figure 15 shows photos of hardware involving in instrument control and data acquisition.

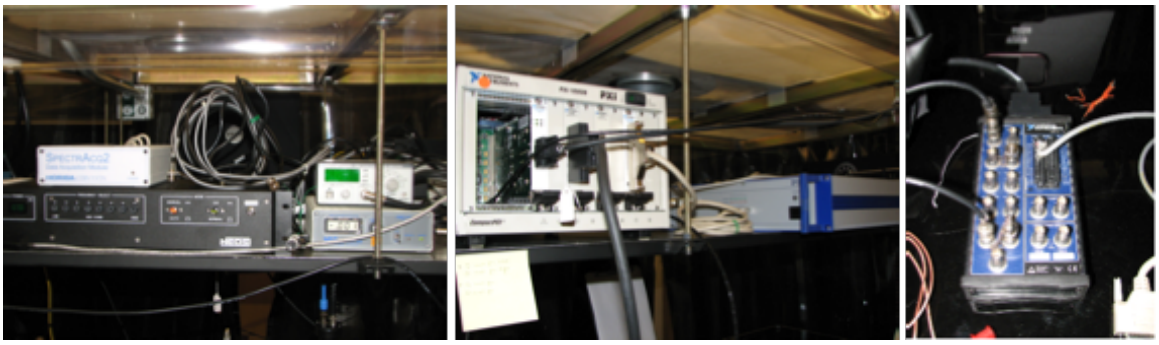

Figure 15: (left) instrument drivers, (middle) data acquisition hardwires, and (right) cabling interfaces.

**Piezo initialization**

Initialization of digital piezo controller and making connection with stage axes. At this step, the controller is identified, axes are referenced, and an error check up will be performed to see that everything is set properly for next steps. Whole the procedure is done through serial port RS232 at highest baud rate. The program is also capable to perform this step by use of GPIB (IEEE-488) communication port, as can be desirable by the user. Diagram is shown below.

**DAQ test**

After initialization of digital piezo controller and connecting piezo stage axes, the program test the data acquisition board, which in our case is NI DAQ 6070E. A check sum is performed and displayed by the program to make sure it is working fine. Working parameters of the board are displayed for advanced users.

**PIO Configure**

Program also configures the parallel input output (PIO) port of the digital piezo controller for fast data acquisition through the DAQ Board NI 6508 by a 96-pin connector. After configuring this port, digital data can be read simultaneously with four steps. The time relation of PIO data write and settling of Piezo Stage position is also shown below:

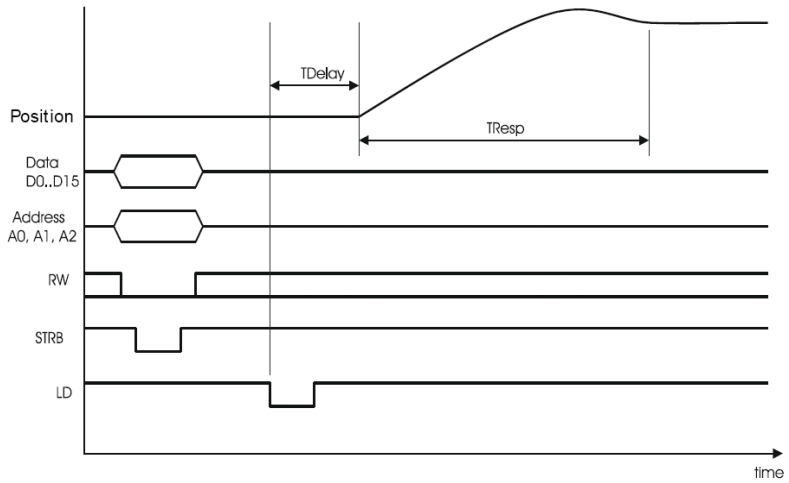


Figure 16: Timing relation of PIO data write and settling of Piezo Stage position.

## Scan XY

Then the program is ready and listening to commands from the front panel. This is the main segment of program. The scanning performs as a raster scan. The block diagram for doing the raster scan, in X and Y directions, is shown in Figure 17.

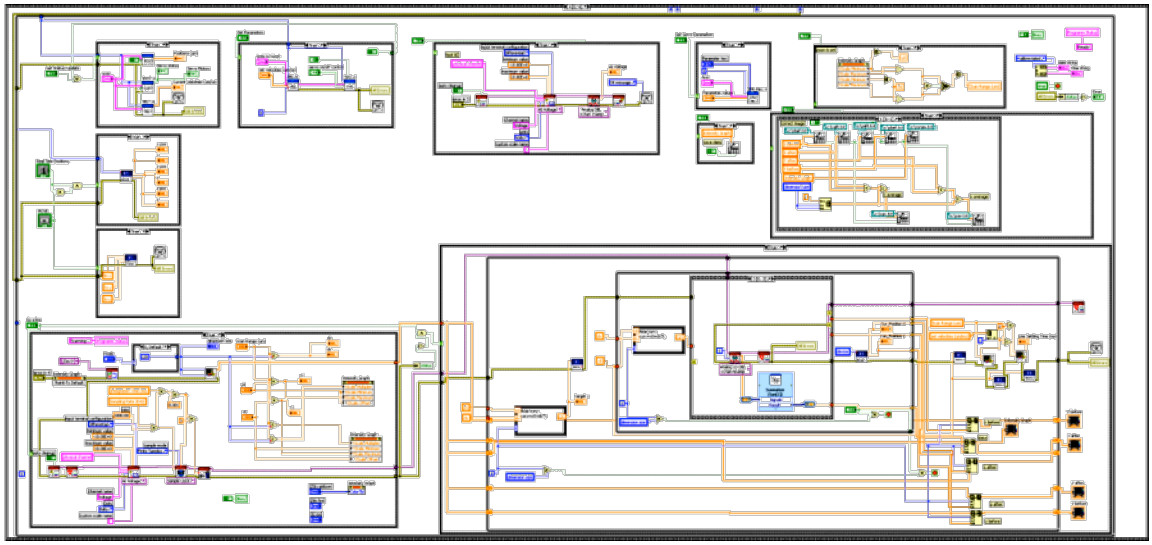

Figure 17: A representative snapshot of the block diagram of XY scanning LabView code.

## Microscope performance

This section highlights the optical performance of our two-photon microscope.

### Resolution target

We have tested the optical aberration of our imaging system using a resolution target and a HeNe continuous-wave laser with a 25-µm pinhole for background discrimination. The left image of

Figure 18 shows the confocal image of resolution target when laser beam suffers from horizontal astigmatism. After we correct the astigmatism, the feature becomes much sharper. The numerical aperture used in this test is 0.4.

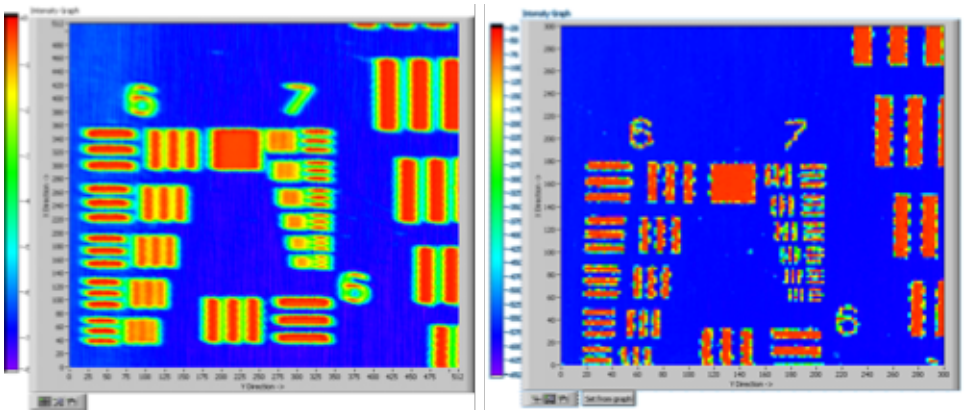


Figure 18: Reflected confocal images of resolution target with (left) and without (right) astigmatism.

## 200-nm fluorescence yellow-green beads

Figure 19 shown two-photon fluorescence image of 200-nm fluorescence yellow-green beads. The excitation wavelength is 800 nm with laser power 10 mW and 1.4-NA Zeiss microscope objective. Both aggregate and single beads are observed.

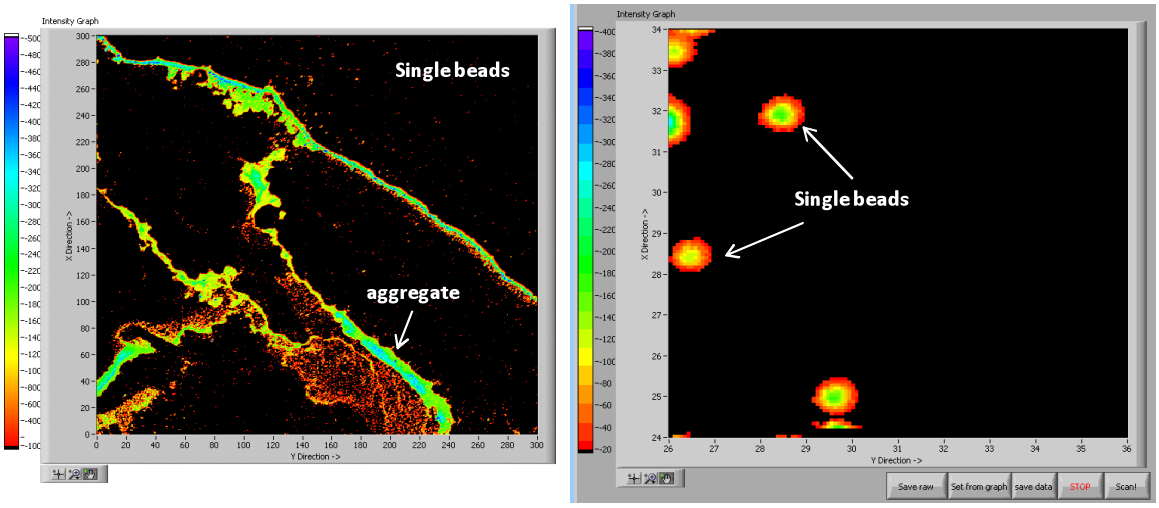


Figure 19: Two-photon fluorescence image of 200-nm fluorescence beads. The image size is (left) 300 μm x 300 μm and (right) 10 μm x 10 μm. Integration time is 5 ms.

## 20-nm fluorescence Nile Red beads

Figure 20 shown two-photon fluorescence image of 20-nm fluorescence yellow-green beads. The excitation wavelength is tuned to 850 nm with laser power 20 mW and 1.4-NA Zeiss microscope objective. Both aggregate and single beads are observed. The single bead image demonstrates the point spread function of laser focus, which is around 250 nm.

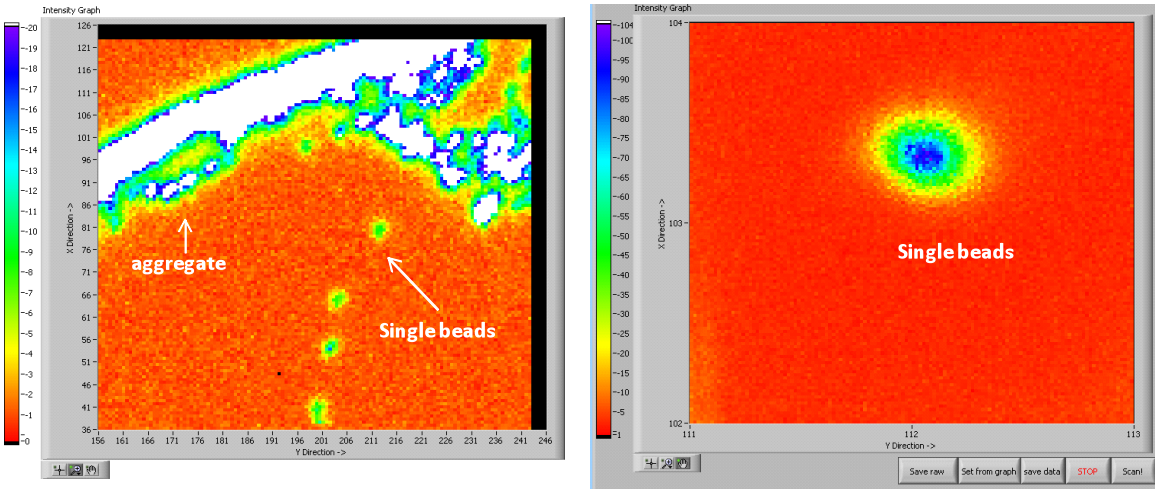


Figure 20: Two-photon fluorescence image of 20-nm fluorescence beads. The image size is (left) 90 μm x 90 μm and (right) 2 μm x 2 μm. Integration time is 5 ms.

## Z-scan

Our piezo scanner can also move along z direction with close loop feedback. Figure 21 shows optical cross sectioning of fluorescence beads with a z step of 1 μm. Clearly the image at the rightmost is close to true laser focus compared to the first three. Notice the astigmatic aberration is observed near laser focus.

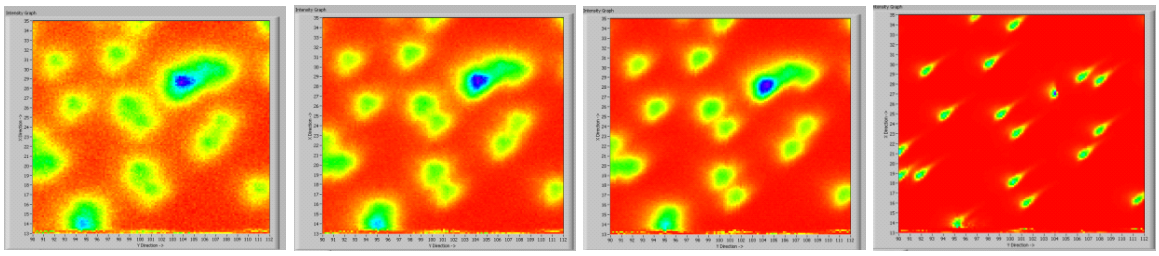

Figure 21: Optical cross section of fluorescence beads with a z step of 1 μm.

**M. A. Fiddy April 30th 2012**